Article:
Jestice, L.H., Butler, L., Lea, R.A. et al. (2026) HDAC6 inhibition alleviates mitochondrial trafficking in novel models of Charcot-Marie-Tooth Disease type 2A. JCI Insight. e200106. ISSN: 2379-3708

https://doi.org/10.1172/jci.insight.200106

JCI insight

HDAC6 inhibition alleviates mitochondrial trafficking in novel models of Charcot-Marie-Tooth Disease Type 2A

Lydia H. Jestice, Larissa Butler, Rebecca A. Lea, Kathryn I. Adamson, Jonas Van Lent, Stuart L. Johnson, Hollie Weedon, Eldriena D'Silva, Gabriele Gelezauskaite, Bob Asselbergh, Eloise Brown, Owen Laing, Christopher J. Price, Dylan Stavish, Anestis Tsakiridis, Mark O. Collins, Vincent Timmerman, Kurt J. De Vos, Alison E. Twelvetrees, Andrew J. Grierson, Ivana Barbaric

JCI Insight. 2026. https://doi.org/10.1172/jci.insight.200106.

Research In-Press Preview **Cell biology** **Neuroscience**

Charcot-Marie-Tooth Disease (CMT) is a group of inherited progressive conditions affecting distal motor and sensory neurons, leading to muscle weakness, pain and loss of sensation in limbs. CMT type 2A (CMT2A) is the most common form of axonal CMT and is associated with a more severe clinical manifestation. However, there are no treatments currently available. To investigate disease mechanisms and facilitate treatment discovery, we developed an in vitro model for CMT2A by introducing the patient-specific $MFN2^{R94Q/+}$ variant into human embryonic stem cells (hESCs). Isogenic variant and wild-type hESCs differentiated to spinal motor neurons with similar efficiency and gave rise to functional motor neurons in vitro. However, $MFN2^{R94Q/+}$ spinal motor neurons displayed impaired mitochondrial trafficking, resulting in altered distribution of mitochondria in axons. Unbiased quantitative proteomic profiling of the endogenous MFN2 interactome revealed dose-dependent remodelling by the R94Q variant across 412 proteins, highlighting candidate mechanisms in disease pathology. Importantly, we showed that mitochondrial trafficking defects could be alleviated by treatment with an HDAC6 inhibitor. Chemical inhibition of HDAC6 also rescued the motor phenotype in a zebrafish CMT2A model. Taken together, our study reveals a variant-specific insight into CMT2A disease mechanisms and confirms HDAC6 as a promising target for further therapeutic development.

HDAC6 inhibition alleviates mitochondrial trafficking in novel models of Charcot-Marie-Tooth Disease Type 2A

Lydia H. Jestice[1,2], Larissa Butler[1,2], Rebecca A. Lea[1,2], Kathryn I. Adamson[2,3,4], Jonas Van Lent[5,6], Stuart L. Johnson[1,2], Hollie Weedon[1,2], Eldriena D'Silva[1,2], Gabriele Gelezauskaite[1,2], Bob Asselbergh[7,8], Eloise Brown[2,3], Owen Laing[1,2], Christopher J. Price[1,2], Dylan Stavish[1,2], Anestis Tsakiridis[1,2], Mark O. Collins[1,2], Vincent Timmerman[5,6], Kurt J. De Vos[2,3], Alison E. Twelvetrees[2,3], Andrew J. Grierson[2,3,4], Ivana Barbaric[1,2,*]

[1] School of Biosciences, The University of Sheffield, Sheffield, United Kingdom

[2] Neuroscience Institute, The University of Sheffield, Sheffield, United Kingdom

[3] Sheffield Institute for Translational Neuroscience, The University of Sheffield, Sheffield, United Kingdom

[4] Bateson Centre, The University of Sheffield, Sheffield, United Kingdom

[5] Peripheral Neuropathy Research Group, Department of Biomedical Sciences, University of Antwerp, Antwerp, Belgium

[6] Laboratory of Neuromuscular Pathology, Institute Born Bunge, Antwerp, Belgium

[7] VIB Center for Molecular Neurology, VIB, Antwerp, Belgium

[8] Department of Biomedical Sciences, University of Antwerp, Antwerp, Belgium

* Corresponding author: Ivana Barbaric: i.barbaric@sheffield.ac.uk

School of Biosciences, The University of Sheffield, Western Bank, Sheffield, S10 2TN, United Kingdom

Conflict of interest statement

The authors report no conflicts of interest in this work.

Abstract

Charcot-Marie-Tooth Disease (CMT) is a group of inherited progressive conditions affecting distal motor and sensory neurons, leading to muscle weakness, pain and loss of sensation in limbs. CMT type 2A (CMT2A) is the most common form of axonal CMT and is associated with a more severe clinical manifestation. However, there are no treatments currently available. To investigate disease mechanisms and facilitate treatment discovery, we developed an in vitro model for CMT2A by introducing the patient-specific *MFN2*$^{R94Q/+}$ variant into human embryonic stem cells (hESCs). Isogenic variant and wild-type hESCs differentiated to spinal motor neurons with similar efficiency and gave rise to functional motor neurons in vitro. However, *MFN2*$^{R94Q/+}$ spinal motor neurons displayed impaired mitochondrial trafficking, resulting in altered distribution of mitochondria in axons. Unbiased quantitative proteomic profiling of the endogenous MFN2 interactome revealed dose-dependent remodelling by the R94Q variant across 412 proteins, highlighting candidate mechanisms in disease pathology. Importantly, we showed that mitochondrial trafficking defects could be alleviated by treatment with an HDAC6 inhibitor. Chemical inhibition of HDAC6 also rescued the motor phenotype in a zebrafish CMT2A model. Taken together, our study reveals a variant-specific insight into CMT2A disease mechanisms and confirms HDAC6 as a promising target for further therapeutic development.

Introduction

Charcot Marie Tooth Disease (CMT) is a group of inherited progressive conditions affecting spinal motor and sensory nerves, resulting in muscle weakness, pain and loss of sensation in limbs of CMT patients (1). Traditionally, CMT is classified into several different types, with the onset of some of the most severe clinical manifestations occurring within the subtype CMT2A (2,3). CMT2A patients typically become wheelchair-reliant by the age of 20 and often exhibit optic atrophy and/or hearing loss (3). CMT2A is caused by variants in Mitofusin 2 (*MFN2*), which encodes a GTPase protein located on the outer mitochondrial membrane (4). MFN2 has several known functions, with a canonical role of mediating the outer membrane fusion of mitochondria (5). Over 140 different variants have been mapped to *MFN2* in CMT2A patients (6-8). A particularly frequent and phenotypically severe form of the disease is caused by an autosomal dominant missense variant leading to the substitution of arginine with either glutamine or tryptophan at the residue 94 of MFN2 (denoted as R94Q and R94W, respectively) (3,7,9). Despite substantial progress in the identification of *MFN2* variants in CMT2A patients, how such variants impact MFN2 function to give rise to the disease phenotype remains poorly understood.

CMT2A involves the progressive degeneration of spinal motor and sensory neurons, exhibiting an axonal length-dependent phenotype. An attractive hypothesis to explain the nerve length-dependent manifestation of CMT2A focuses on aberrant mitochondrial trafficking through axons (10,11). This is supported by a seminal study in cultured rat dorsal root ganglion (DRG) neurons expressing a variant form of MFN2 which demonstrated an abnormal clustering of mitochondria in neuronal cell bodies and proximal axons as well as reduced mitochondrial mobility in variant cells (12). Subsequent studies in other in vivo and in vitro models of CMT2A, including zebrafish and mouse (13,14), further supported the links between impaired mitochondrial trafficking and *MFN2* variants. Consequently, rescuing axonal

70 trafficking of mitochondria has been highlighted as a promising therapeutic strategy for the
71 treatment of CMT2A (15).

72 HDAC6 inhibition has been shown to effectively alleviate motor and sensory defects
73 in a mouse model of CMT2A thought to be due to an increase in α-tubulin acetylation in
74 peripheral nerves of variant mice (16,17). Similar studies utilising HDAC6 inhibition in CMT
75 type 2D and CMT type 2F mouse models showed comparable rescues of motor and sensory
76 deficits as well as restoring axonal transport deficits (18,19). Moreover, HDAC6 inhibitors
77 proved effective in alleviating mitochondrial transport in models of other neurodegenerative
78 diseases whose pathology is also linked to mitochondrial trafficking, such as amyotrophic
79 lateral sclerosis (20,21). Together, these observations suggest that the HDAC6 inhibition may
80 provide a much-needed therapeutic option for neurodegenerative diseases underpinned by
81 mitochondrial transport defects. Nevertheless, the therapeutic efficacy of HDAC6 inhibition in
82 the context of CMT2A requires further investigation utilising human-based and additional
83 physiologically relevant animal disease models.

84 The selective vulnerability of spinal motor neurons to CMT2A necessitates the use of
85 disease-relevant cell types for the investigation of MFN2 disease-associated dysfunction and
86 for testing approaches for alleviating the disease phenotype. While human spinal motor neurons
87 are experimentally inaccessible, the advent of human pluripotent stem cell (hPSC) technology
88 has offered a means to derive them in vitro (22,23). HPSCs, which encompass both human
89 embryonic stem cells (hESCs) derived from early blastocysts (24) and induced pluripotent stem
90 cells (hiPSC) reprogrammed from somatic cells (25), have the ability to differentiate to any
91 cell type (24,25). Here, we introduced the patient-specific variant *MFN2*$^{R94Q/+}$ into hESCs to
92 obtain isogenic variant and wild-type cells and we established a robust protocol for
93 differentiation of hESCs to disease-relevant spinal motor neurons. We show that impaired
94 mitochondrial trafficking and altered mitochondrial distribution are the key features of

MFN2$^{R94Q/+}$ motor neurons. To identify candidate molecular mechanisms underlying these defects, we performed unbiased quantitative proteomic profiling of the endogenous MFN2 interactome across isogenic *MFN2*$^{+/+}$, *MFN2*$^{R94Q/+}$, and *MFN2*$^{R94Q/R94Q}$ hESCs, revealing broad and dose-dependent remodelling of the MFN2 interaction network by the R94Q variant. We further showed that mitochondrial trafficking defects in *MFN2*$^{R94Q/+}$ motor neurons could be reversed by chemically inhibiting HDAC6. Finally, to demonstrate the in vivo relevance of these findings, we chemically inhibited HDAC6 in a zebrafish *mfn2* variant (13). This significantly rescued their aberrant swimming phenotype, thus confirming HDAC6 as a promising therapeutic target in CMT2A.

Results

Generation of isogenic *MFN2*$^{R94Q/+}$ and *MFN2*$^{+/+}$ hESCs

We set out to generate a human cell-based model of CMT2A by introducing one of the most common and phenotypically severe CMT2A-causing missense variant, *MFN2*$^{R94Q/+}$, into the hESC line MShef11 (26). To this end, we transfected euploid early-passage hESCs with a Cas9-guide RNA duplex along with a repair template designed to introduce the c.G281A substitution into the *MFN2* gene. To generate clonal lines, bulk transfected cells were single-cell sorted and expanded (Figure 1A). The resulting hESC colonies were subsequently screened for successful editing by Sanger sequencing of the target region. Following the screening, four heterozygous edited clones from two independent rounds of editing were single-cell sorted again and sub-clones (from herein termed Het1, Het3.1, Het3.2, and Het4) were identified, sequenced, and expanded for in-depth analyses (Figure 1B). As control cells in phenotypic assays, we used wild-type parental cells (termed WT1) and an unedited wild-type clone that had undergone CRISPR/Cas9 transfection (termed WT2) (Figure 1A, B). All of the lines remained karyotypically diploid (Supplementary Figure 1A) and did not harbour any predicted off-target variants arising during CRISPR/Cas9 mutagenesis (Supplementary Figure 1B**)**. Introduction of the heterozygous variant did not affect MFN2 protein expression in the clones (Figure 1C). These lines also retained their undifferentiated hESC phenotype post-editing, as evidenced by colony morphology (Supplementary Figure 2A), and expression of key pluripotency-associated markers (Figure 1D; Supplementary Figure 2B, 2C). They also retained their pluripotency, demonstrating similar efficiency in differentiation to cells of the three primary germ layers as their parental line (Supplementary Figure 2D, 2E). Overall, the CRISPR/Cas9 editing of hESCs enabled us to generate isogenic lines with and without *MFN2*$^{R94Q/+}$ heterozygous variant for CMT2A disease modelling.

MFN2$^{R94Q/+}$ hESCs efficiently differentiate into functional spinal motor neurons

To model CMT2A in vitro, we aimed to produce spinal motor neurons from *MFN2*$^{R94Q/+}$ hESCs. During development, limb-innervating spinal motor neurons arise in the brachial and lumbar-level spinal cord (27). They are characterised by high expression of MNX1 (HB9) (28), in addition to the expression of motor neuron markers (e.g. choline acetyltransferase (CHAT), ISLET-1/2, OLIG2, and FOXP1) (29,30). Depending on their axial level, limb-innervating motor neurons express different HOX paralogous group (PG) genes. For example, brachial motor neurons express HOX PG 6, with HOX PG 5 expressed rostrally and HOX PG 8 caudally (31), whereas lumbar motor neurons express HOX PG 10 (31).

Hence, to develop an efficient protocol for forelimb-innervating spinal motor neuron differentiation, we modified previously published protocols for neural differentiation from hESCs (21,32) (Figure 2A). We then utilised the protocol to ascertain whether the *MFN2*$^{R94Q/+}$ variant impacts the differentiation of hESCs to spinal motor neurons. We subjected *MFN2*$^{R94Q/+}$ hESCs, alongside the *MFN2*$^{+/+}$ WT1 and WT2 cells, to our optimised differentiation protocol (Figure 2B, Supplementary Figure 3). To compare the differentiation efficiency of *MFN2*$^{R94Q/+}$ hESCs versus *MFN2*$^{+/+}$ cells, we quantified the number of cells expressing different markers, including (motor) neuron markers (MNX1 (HB9), ISL1/2, CHAT) at day 34 of the differentiation protocol by immunofluorescence (Figure 2C; Supplementary Figure 4A-D) and RT-qPCR (Figure 2D; Supplementary Figure 4E-K). All of the populations exhibited a similar overall trend in the expression of key markers of motor neuron identity and there were no significant differences in the differentiation efficiency of *MFN2*$^{R94Q/+}$ cells compared with *MFN2*$^{+/+}$ hESCs. Moreover, a robust expression of *HOXB5*, *HOXB6*, and *HOXB7* indicated the acquisition of a predominantly brachial identity by spinal motor neurons in all cell populations (Supplementary Figure 4L-Q).

Finally, we assessed the functional properties of hESC-derived motor neurons at day

34 to 36 of differentiation. Motor neurons were found to be electrophysiologically active based on analysis of action potential activity and ionic currents using patch-clamping, with no overt differences observed between *MFN2*$^{+/+}$ and *MFN2*$^{R94Q/+}$ motor neurons (Figure 2E-G; Supplementary Figure 5A-C). Taken together, this data demonstrates that the *MFN2*^{R94Q} variant does not impact the differentiation efficiency or electrophysiological properties of hESC-derived spinal motor neurons at day 34-36 of differentiation.

Altered mitochondrial morphology and distribution of mitochondria in axons of *MFN2*$^{R94Q/+}$ spinal motor neurons

Since MFN2 is critical for mitochondrial fusion, and mitochondrial morphology is directly influenced by MFN2-mediated fusion, we first examined the potential impact of the *MFN2*$^{R94Q/+}$ variant on mitochondrial morphology. To this end, we performed high-resolution imaging of mitochondria within hESC-derived motor neurons. After 34 days of differentiation, we transfected motor neurons with a construct encoding a mitochondrial targeting sequence fused to a red fluorescent protein (Mito-DsRed2) in combination with another construct encoding enhanced green fluorescent protein (eGFP). Only a small proportion of neurons were labelled with both eGFP and Mito-DsRed2, thus enabling us to identify mitochondria within individual axons of densely populated motor neuron cultures (Supplementary Figure 6A, 6B). Compared to control neurons, we observed a striking reduction of mitochondrial size in *MFN2*$^{R94Q/+}$ neurons (Figure 3A). Quantitative analysis revealed that mitochondrial area (Figure 3B) and length (Figure 3C) were significantly decreased specifically in the distal portions of *MFN2*$^{R94Q/+}$ neurons compared to *MFN2*$^{+/+}$ neurons. To validate these findings, we examined an independent alternative iPSC-derived model of MFN2-related neuropathy, also carrying the R94Q variant, originating from CMT2A patient material (33). A different differentiation protocol was used in this existing iPSC-line to produce ISLET-1-positive and

MNX1 (HB9)-positive motor neurons (Supplementary Figure 6C, 6D), then we imaged and quantified mitochondrial size in proximal and distal axonal zones with an alternative methodology. This independent model also showed a similar phenotype, with reduced mitochondrial size in the distal portions of *MFN2*$^{R94Q/+}$ axons (Supplementary Figure 7A, 7B).

In addition to altered mitochondrial morphology, we noted a prominent increase in the overall spacing between mitochondria in *MFN2*$^{R94Q/+}$ motor neuron axons, as measured by the number of mitochondria per 100 μm (Figure 3D). The increased spacing between mitochondria in *MFN2*$^{R94Q/+}$ motor neuron axons argues against a primary defect in mitochondrial fusion. Instead, this increased spacing, especially in conjunction with the more severe distal morphological changes, is consistent with impaired mitochondrial transport to distal axonal regions.

MFN2$^{R94Q/+}$ impairs mitochondrial trafficking in hESC-derived spinal motor neurons

MFN2 has been reported to have a role in axonal transport, with loss of protein resulting in a reduction in motile mitochondria in the axon (34). Variants in *MFN2* have also been shown to impact axonal transport (12,33). To directly test the hypothesis that *MFN2*$^{R94Q/+}$ impacts mitochondrial axonal transport in our model of CMT2A, we performed time-lapse microscopy of mitochondrial movement within the axons of *MFN2*$^{R94Q/+}$ and *MFN2*$^{+/+}$ motor neurons (Figure 4A; Supplementary Movie S1, S2). Kymographs generated from time-lapse videos were analysed for potential differences in motility of mitochondria in *MFN2*$^{R94Q/+}$ and *MFN2*$^{+/+}$ motor neurons (Figure 4A; Supplementary Figure 8). We considered mitochondria motile if they moved with a speed of over 0.3 μm/s, as movements below this threshold could be attributed to actin-mediated transport (35). We found that the mitochondria in *MFN2*$^{R94Q/+}$ hESC-derived motor neurons were significantly less motile compared to controls. Specifically,

the percentage of motile mitochondria in *MFN2*$^{R94Q/+}$ neurons was reduced to 3.5±4.6% (mean±SD) compared to 15.3±13.7% in wild-type neurons (Figure 4B). This represents an approximate 77% reduction in overall mitochondrial motility in variant cells, with their transport, as measured by percentage motility, reduced in both anterograde and retrograde directions (Figure 4C, 4D; Supplementary Figure 9A, 9B).

Whole-track velocity analysis of motile tracks revealed no significant difference in the average speed of motile mitochondria in either the anterograde or retrograde direction between *MFN2*$^{R94Q/+}$ and wild-type motor neurons (Figure 4E, 4F). This suggests that the overall speed of mitochondrial movement is not grossly affected by the *MFN2*$^{R94Q/+}$ variant. Further analysis of instantaneous velocity, which reflects the speed of mitochondria at specific time points (Figure 4G, 4H; Supplementary Figure 9C, 9D), revealed an increase in speed in both the anterograde and retrograde direction. This apparent discrepancy of whole-track and instantaneous velocity can be reconciled by considering the possibility of increased pausing events of mitochondria in *MFN2*$^{R94Q/+}$ neurons. Increased pausing can indicate that mitochondria are unable to sustain continued or optimal movement speeds and is therefore associated with mitochondrial transport dysfunction. In our analysis, mitochondrial pausing was defined as a transient cessation of mitochondrial movement that lasted at least 3 frames before a mitochondrion restarted movement at a speed higher than 0.3 μm/s. The length of pauses within motile tracks was calculated for *MFN2*$^{+/+}$ and *MFN2*$^{R94Q/+}$, and *MFN2*$^{R94Q/+}$ motile mitochondria exhibited longer pauses on average compared to *MFN2*$^{+/+}$ motile mitochondria (Figure 4I). Together, these findings strongly support the notion that mitochondrial transport was more frequently interrupted in the *MFN2*$^{R94Q/+}$ neurons, with mitochondria frequently pausing and changing direction, potentially due to impaired interactions with the motor proteins or the microtubule network.

Finally, to determine the cell-type specificity of the observed transport defects, we

investigated enteric neurons derived from the same isogenic hESC lines via a vagal neural crest intermediate (36,37) (Supplementary Figure 10A). Notably, *MFN2*$^{R94Q/+}$ enteric neurons exhibited no significant reduction in mitochondrial motility compared to *MFN2*$^{+/+}$ controls (Supplementary Figure 10B). These findings suggest that the mitochondrial trafficking deficit is not a generalized neuronal phenomenon but may represent a selective vulnerability of spinal motor neurons, consistent with the clinical presentation of CMT2A.

Quantitative Proteomic Screening Identifies Candidate Regulators of Mitochondrial Trafficking

To investigate the impact of the R94Q variant on the MFN2 interactome, we performed immunoprecipitation of endogenous MFN2 followed by data-independent acquisition mass spectrometry (DIA-MS) in three isogenic hESC lines: *MFN2*$^{+/+}$, *MFN2*$^{R94Q/+}$, and *MFN2*$^{R94Q/R94Q}$ (Figure 5A). Although the homozygous R94Q variant is not observed in CMT2A patients, we reasoned that the homozygous genotype would reveal proteomic alterations that might remain sub-threshold for detection in heterozygous *MFN2*$^{R94Q/+}$ cells.

The screen quantified 4,299 protein groups, of which 644 were significantly enriched in *MFN2*$^{+/+}$ immunoprecipitations over IgG (Supplementary Table S1). Our proteomic workflow showed high reproducibility across three biological replicates (median Pearson r=0.98) (Figure 5B), and principal component analysis clearly separated MFN2 immunoprecipitations from IgG controls (Figure 5C). The screen recovered 16 of the 17 MFN2 interactors annotated in BioGRID (38) that were detected in our dataset (Supplementary Table S1), supporting the specificity of the immunoaffinity purification. These included MFN2's fusion partner MFN1, the outer membrane import component SAMM50, the E3 ligase HUWE1, and components of the mitochondrial transport and tethering machinery, including

RHOT2 (MIRO2), and MYO19, as well as the cytoskeletal proteins KIF14 and MYH10. Together, these data indicate that our approach efficiently captured a representative cross-section of the endogenous MFN2 interactome.

Next, we investigated the impact of the R94Q variant on the MFN2 interactome by comparing proteins with differential MFN2 association across genotypes. To account for modest differences in MFN2 recovery across biological replicates, all values were bait-corrected (Supplementary Table S1). Pairwise comparison of *MFN2*$^{R94Q/R94Q}$ versus *MFN2*$^{+/+}$ identified 412 proteins with significantly reduced MFN2 association and 6 candidates with significantly increased association (Figure 5D). While the *MFN2*$^{R94Q/+}$ versus *MFN2*$^{+/+}$ comparison was underpowered at the single protein level, the proteins with reduced MFN2 association showed a clear dose-dependent pattern across the isogenic allele series, consistent with the simultaneous co-purification of wild-type and R94Q MFN2 binding partners from heterozygous lysates. Specifically, 410 out of 412 candidates with reduced MFN2 association in *MFN2*$^{R94Q/R94Q}$ cells also showed a matching downward trend in *MFN2*$^{R94Q/+}$ cells (Figure 5E; Supplementary Table S1).

To assess the biological relevance of these candidates, we searched the literature for known functions of the proteins with reduced MFN2 association. We note that unbiased co-immunoprecipitation proteomics will inevitably identify proteins that are unlikely to interact with MFN2 in a biologically meaningful context, including nuclear and transcriptional machinery components whose subcellular localisation is incompatible with direct interaction with an outer mitochondrial membrane protein. We therefore focused our interpretation on candidates with subcellular localisations and known functions compatible with MFN2 biology, with the full dataset provided in Supplementary Table S1 as a resource for future investigation. Among the most notable individual hits with reduced interaction were MARCHF5, a

mitochondrial outer-membrane E3 ligase that regulates MFN2 turnover and ER-mitochondria contacts (39), ATG7, an E1-like autophagy enzyme required for autophagosome biogenesis (40,41), and BNIP3, a mammalian Atg32 homologue that mediates mitophagy (42), suggesting a potential disruption to mitochondrial quality control in variant cells. We also noted reduced association of factors with reported roles in axonal transport and cytoskeletal regulation, including CDK5, a kinase that modulates axonal transport of vesicles and organelles (43,44), TAOK2, which coordinates ER-microtubule tethering (45), and TBCB, a tubulin-specific chaperone that regulates microtubule dynamics (46).

Beyond individual candidates, Gene Ontology enrichment analysis of the 412 proteins with reduced MFN2 association in homozygous R94Q cells, performed against a background of all proteins detected in the mass spectrometry experiment, identified actin cytoskeleton organisation as the most significantly enriched biological process term (34 proteins, FDR = 1.47×10^{-6}), followed by cell migration (30 proteins, FDR = 2.42×10^{-5}), and endocytosis (25 proteins, FDR = 7.39×10^{-5}) (Figure 5F). The actin cytoskeleton organisation term was driven by a functionally diverse set of proteins including cytoskeletal regulators with established roles in axonal biology (CDK5, TMOD3, VASP, COBL), Rho GTPase signalling components (CDC42, ARHGEF17, ARHGAP8, FMNL2), and the non-muscle myosin heavy chains MYH9 and MYH10. These findings raise the possibility that the R94Q variant disrupts MFN2 association with actin cytoskeletal regulatory machinery, potentially impairing actin-based mitochondrial anchoring in addition to microtubule-dependent transport, although validation in a neuronal context will be required to establish the pathological relevance of these interactions. Collectively, these data reveal that the R94Q substitution broadly remodels the MFN2 interactome and provide a hypothesis-generating resource for future mechanistic investigation of how the *MFN2*$^{R94Q/+}$ variant drives selective vulnerability in motor neurons.

HDAC6 inhibition rescues tubulin acetylation and improves mitochondrial trafficking in *MFN2*$^{R94Q/+}$ hESC-derived spinal motor neurons

Several studies pointed to HDAC6 inhibition as a promising approach to alleviating mitochondrial trafficking defects (18,21,47). However, the efficacy of HDAC6 inhibition in alleviating trafficking impairment underpinned by *MFN2*^{R94Q} in human neurons remains unknown. Here, we utilised our hESC-derived *MFN2*$^{R94Q/+}$ spinal motor neurons to test the effect of a selective HDAC6 inhibitor, ACY-738 (48), on mitochondrial trafficking within axons.

MFN2$^{R94Q/+}$ hESC-derived motor neurons and their *MFN2*$^{+/+}$ counterparts were transfected with the Mito-DsRed2 plasmid and the eGFP plasmid and were treated for 24h with 100 nM ACY-738. We confirmed that the ACY-738 treatment increased the amount of acetylated α–tubulin in treated cells (Figure 6A). The effect of treatment on mitochondrial transport was determined by imaging of DsRed2-labelled mitochondria by time-lapse microscopy. Strikingly, tracking of mitochondria revealed an increase in the percentage of motile mitochondria in ACY-738-treated *MFN2*$^{R94Q/+}$ cells (Figure 6B, 6C). The effect of ACY-738 treatment was apparent for both anterograde (Figure 6D; Supplementary Figure 11A) and retrograde (Figure 6E; Supplementary Figure 11B) movement of mitochondria within *MFN2*$^{R94Q/+}$ axons. Furthermore, the length and area of *MFN2*$^{R94Q/+}$ mitochondria in the distal portions of the axons were significantly increased following treatment (Figure 6F, 6G), suggesting that restored trafficking facilitates distal fusion events. To ensure these effects were not confounded by cytotoxicity, we quantified the apoptotic marker cleaved caspase-3. No significant induction of apoptosis was observed (Supplementary Figure 12A-C), indicating that the dose is well-tolerated.

To verify that these improvements were driven by α-tubulin acetylation, we targeted an alternative deacetylase using the SIRT2 inhibitor, AGK2 (49). Similar to HDAC6 inhibition,

SIRT2 inhibition increased tubulin acetylation (Supplementary Figure 13A), and the percentage of motile mitochondria in *MFN2*$^{R94Q/+}$ motor neurons (Supplementary Figure 13B), further supporting the role of microtubule acetylation in facilitating axonal transport in this context. Together, these data demonstrate that pharmacological modulation of microtubule acetylation can bypass transport defects in CMT2A motor neurons.

Chemical inhibition of HDAC6 rescues motor defects in MFN2 variant zebrafish

To investigate whether the potential beneficial effect of HDAC6 inhibition in cultured *MFN2*$^{R94Q/+}$ human motor neurons translates to the more complex physiological situation in vivo, we utilised a zebrafish CMT2A model. We previously showed that *mfn2* variant zebrafish carrying a null allele show a progressive motor phenotype associated with impaired mitochondrial transport and degeneration of the distal axon (13). We performed *mfn2*$^{hu3528/+}$ in-crosses and randomly separated the offspring into two treatment groups which were housed in separate tanks that were not connected to the recirculating water system in the aquarium. From 8 days post fertilisation, the control group were accommodated in tank water containing 2% DMSO and the treatment group were housed similarly, but the tank water also contained 300 nM ACY-738. To minimise the possibility of off-target and toxic effects, an intermittent dosing strategy was used, alternating ACY-738/vehicle-treated water with untreated water on a bi-weekly basis. Despite these modifications, we noticed that the zebrafish housed in these tanks developed at a much slower rate than those maintained on the recirculating aquarium system.

Oral dosing of vehicle or ACY-738 was commenced in the diet from 80 days post fertilisation, and was also administered on an intermittent basis, alternating with untreated food on the same bi-weekly schedule as the immersion treatment. The vehicle treatment group were fed 16 mg of gelly belly diet twice per day, and the treatment group were fed 16 mg of gelly belly diet containing 0.058% (w/w) ACY-738 twice per day. To determine effects of treatment

on motor function, we investigated the critical swimming velocity (Ucrit) of ACY-738- and vehicle-treated fish at monthly intervals between 5- and 7-months post fertilisation, with Ucrit calculated for both treatment groups at each time-point. From 6 months, the Ucrit of ACY-738-treated fish was significantly increased compared to the *mfn2*$^{hu3528/hu3528}$ variants, indicating that ACY-738 treatment improved the defective swimming phenotype (Figure 6H). At 7 months, the experiment was terminated on welfare grounds, as the vehicle treatment animals were showing signs of distress. This result shows that ACY-738 treatment restores defective swimming in a zebrafish CMT2A model.

Discussion

To date there are no approved treatments for CMT2A. Further mechanistic understanding of the disease is required to identify targets that may alleviate disease symptoms. Reliable disease models that recapitulate key features of the disease phenotype are critical for deciphering disease pathophysiology and uncovering therapeutic options. In this study, we capitalised on hESC technology to establish an isogenic human cell-based model of CMT2A. To this end, we combined CRISPR/Cas9 genome editing and directed differentiation of hESCs to derive isogenic spinal motor neurons harbouring one of the most prevalent and phenotypically severe CMT2A-causing variants, *MFN2*$^{R94Q/+}$. We then utilised this cell-based model to analyse CMT2A disease mechanism and test a pharmacological approach to alleviating the disease phenotype.

Our findings demonstrate that *MFN2*$^{R94Q/+}$ motor neurons exhibit significant defects in mitochondrial transport. Specifically, we observed a reduction in the percentage of motile mitochondria compared to wild-type controls paired with an axonal location-dependent reduction in mitochondrial size, indicating impaired mitochondrial trafficking. This finding is consistent with previous observations in a complementary human induced pluripotent stem cell (hiPSC)-based model of CMT2 (33), which we also further analysed in our study (Supplementary Figure 7A, B). A significant strength of our approach is the use of an isogenic hESC-based system, which isolates the pathogenic effects of MFN2 R94Q variant from the potentially confounding influence of individual genetic backgrounds or line-to-line variations. To ensure that our findings were a true reflection of the variant effect and not unique to a single genomic context, we cross-validated our observations in an independent, patient-derived hiPSC model carrying the same R94Q variant (Supplementary Figure 7). The consistent observation of mitochondrial phenotypes across these two models—despite the use of different differentiation protocols and distinct genetic origins—underscores the robustness of

mitochondrial transport impairment as a hallmark of MFN2 R94Q pathology. Our dual-model approach demonstrated clear consistency between engineered hESCs and patient hiPSCs, reinforcing the physiological relevance of our findings and suggesting that the R94Q variant in these cells exerts a pervasive effect on mitochondrial dynamics irrespective of individual genetic background.

To dissect the underlying mechanisms of mitochondrial transport impairment, we analysed mitochondrial motility dynamics in detail. Whole-track velocity was unchanged by *MFN2*$^{R94Q/+}$ but *MFN2*$^{R94Q/+}$ mitochondria spent more time paused. We explained this discrepancy by noting that *MFN2*$^{R94Q/+}$ mitochondria had increased instantaneous velocity, such that faster movements with more pauses averaged out to a similar whole-track velocity as *MFN2*$^{+/+}$ neurons. The pausing of transport could be attributed to several different causes including altered intracellular calcium concentrations (50), motor protein dissociation from the microtubules (51), or motor protein dissociation from the intracellular cargo of interest (52). To our knowledge, this is the first model to show increases in anterograde instantaneous velocity of mitochondria in the presence of a CMT2A-causing variant, and this increase may be attributed to increased kinesin-1 processivity or a greater contribution of other kinesin motor proteins, such as kinesin-3, which can achieve greater speeds than kinesin-1 (53,54). Taken together, this analysis of transport dynamics is suggestive of a disruption to the ability of motor proteins to carry out their function efficiently.

To investigate the biochemical basis of this disrupted motor function, we performed quantitative immunoprecipitation–mass spectrometry on MFN2's endogenous interactome across the isogenic allele series. Our analysis identified 412 partners with significantly reduced MFN2 association in *MFN2*$^{R94Q/R94Q}$ cells. The majority of candidates showed concordant downward trends in heterozygous *MFN2*$^{R94Q/+}$ cells, indicating dose-dependent disruption of

409 the MFN2 interactome. Among the candidates with reduced MFN2 association, several are of
410 particular functional relevance. MARCHF5, a mitochondrial outer-membrane E3 ubiquitin
411 ligase that regulates MFN2 turnover and ER–mitochondria tethering, modulates the local pool
412 of MFN2 available for adapter engagement (39). CDK5 is a known regulator of axonal
413 transport (43,44), providing a plausible biochemical basis for the altered motor engagement
414 implied by our motility analysis. Additionally, the mitophagy machinery components ATG7
415 (40,41), and BNIP3 (42), were among the reduced interactors, raising the possibility that
416 variant-driven interactome remodelling impairs not only mitochondrial transport but also the
417 quality control mechanisms responsible for clearing dysfunctional mitochondria from axons, a
418 process of particular importance in the distal regions of long motor neuron axons. Gene
419 Ontology enrichment analysis of the 412 reduced interactors independently identified actin
420 cytoskeleton organisation as the most significantly enriched biological process term. These
421 findings raise the possibility that the R94Q variant disrupts MFN2 association with actin
422 cytoskeletal regulatory machinery. Given the multiple roles of actin in mitochondrial biology,
423 including anchoring, fission, and fusion, the functional consequences of this disruption may
424 extend beyond trafficking, although validation in a neuronal context will be required to
425 establish the pathological relevance of these interactions. Taken together, the dose-dependent
426 loss of interactions spanning MFN2's regulatory, transport, cytoskeletal, and quality control
427 networks supports a model in which the R94Q substitution broadly destabilises the MFN2
428 interactome in a manner consistent with the mitochondrial trafficking defects observed in
429 $MFN2^{R94Q/+}$ motor neurons. We emphasise that this dataset identified candidate mechanisms
430 rather than established causal pathways, and prioritised follow-up of identified candidates will
431 be required to determine which specific interactome changes drive the observed trafficking
432 deficits.

A defining feature of CMT2A is the selective vulnerability of long-axon motor neurons despite the ubiquitous expression of MFN2. To investigate whether the trafficking defect we observed reflects a generalised neuronal phenomenon or a lineage-restricted vulnerability, we differentiated our isogenic hESC lines into enteric neurons, a population that is not known to be involved in CMT2A clinical manifestation. *MFN2*$^{R94Q/+}$ enteric neurons differentiated efficiently and maintained mitochondrial motility levels comparable to wild-type controls (Supplementary Figure 10A, 10B). The selective vulnerability of spinal motor neurons in our model therefore mirrors the clinical presentation of CMT2A, suggesting that the R94Q variant interacts with cell-type-specific factors, potentially including the unique metabolic demands, axonal geometry, or cytoskeletal organisation of long-projection motor neurons, to produce its pathogenic effect.

Finding a drug that rescues an aberrant motor neuron phenotype could provide a platform for developing pharmacological treatments for CMT2A patients. Based on our identification of aberrant mitochondrial trafficking as a key phenotype in CMT2A human motor neurons, we focused on finding a drug that could revert this aberration. Mitochondrial axonal transport can be increased by treatment of neurons with HDAC6 inhibitors, which are thought to mediate their effects on mitochondrial trafficking through increasing acetylation of tubulin (19,21,47,55). No loss of acetylation was noted in untreated *MFN2*$^{R94Q/+}$ motor neurons whereas other murine-based models in the literature have shown disruption to tubulin acetylation in the presence of CMT2A-associated variants (16,56). Using an HDAC6 inhibitor ACY-738, we showed a partial reversion of the diseased phenotype, as ACY-738-treated *MFN2*$^{R94Q/+}$ cells exhibited increased percentage of motile mitochondria compared to non-treated *MFN2*$^{R94Q/+}$ motor neurons, and mitochondrial length and area in the distal axon were significantly increased following treatment, suggesting that restored trafficking enables the distal fusion events necessary to maintain healthy organelle morphology. To confirm whether

458 this effect was clinically relevant, we tested ACY-738 in a zebrafish CMT2A model with loss
459 of function of mfn2, where it significantly alleviated motor phenotypic defects. The
460 convergence of rescue effects across a human cell-based model and an in vivo vertebrate
461 system strengthens confidence in HDAC6 inhibition as a promising therapeutic strategy for
462 CMT2A and supports its progression towards pre-clinical development. Importantly, SIRT2
463 inhibition also restored mitochondrial motility in *MFN2*$^{R94Q/+}$ motor neurons, confirming that
464 the rescue effect is attributable to increased tubulin acetylation rather than an off-target effect
465 of ACY-738 specifically.

466 Several limitations of the present study should be acknowledged. First, whilst HDAC6
467 inhibition with ACY-738 partially restored mitochondrial motility in *MFN2*$^{R94Q/+}$ motor
468 neurons, the rescue was incomplete, and the long-term functional consequences of this
469 treatment on neuronal survival, axonal integrity, and synaptic activity were not investigated.
470 These represent important outcomes for future pre-clinical assessment, alongside a
471 comprehensive long-term safety profiling of ACY-738, which extends beyond the scope of the
472 present study. Second, whilst our data establish impaired mitochondrial trafficking as a
473 prominent and reproducible phenotype in *MFN2*$^{R94Q/+}$ motor neurons, whether this represents
474 the primary pathogenic driver or a secondary consequence of broader mitochondrial
475 dysfunction remains an open question that cannot be resolved from the current dataset alone.
476 Addressing this issue will require longitudinal studies integrating additional functional
477 readouts, including ATP production, mitochondrial membrane potential, calcium buffering
478 capacity, and markers of axonal degeneration. Third, the zebrafish rescue experiments
479 employed a *mfn2* null model rather than the specific R94Q variant, limiting direct genotypic
480 equivalence with the human in vitro model. We note, however, that genotype-specific evidence
481 is provided by our isogenic hESC system, whereas the zebrafish experiments provide
482 complementary in vivo proof of concept for the therapeutic approach. Fourth, the selective

vulnerability of spinal motor neurons was inferred from a comparison with enteric neurons, a population not associated with the clinical manifestations of CMT2A. Whilst this comparison provides initial evidence for lineage-restricted vulnerability, the evaluation of additional neuronal subtypes will be required to strengthen this conclusion. Finally, our proteomic data identified disruption of MFN2 association with the actin cytoskeletal regulatory machinery as a candidate pathological mechanism; however, we acknowledge that this conclusion is speculative in the absence of direct experimental validation of actin-dependent mitochondrial anchoring or transport in a neuronal context, and that the enrichment of actomyosin components may partly reflect the hESC cellular context in which the screen was performed. Together, these limitations define a clear agenda for future investigation building on the core findings of this study, which establish impaired mitochondrial trafficking as a defining feature of *MFN2*$^{R94Q/+}$ motor neurons and identify HDAC6 inhibition as a promising therapeutic strategy warranting further development.

Materials and Methods

Sex as a variable

Zebrafish sex determination happens at 20-30 days post fertilisation, and sex can be determined using externally visible phenotypes by 3-4 months of age. The zebrafish used in this study were sexed and genotyped at 4 months of age, and at this stage sex- and treatment-matched experimental groups for behavioural analysis were determined.

Human pluripotent stem cell maintenance

The hESC line used in this study was the MShef11 human embryonic stem cell line (RRID: CVCL_BW83) (26). A working bank of MShef11 was made from cells around 20 passages from the original derivation. In this study, cells were defrosted from a working bank and were grown for no longer than 10 passages from defrosting. Cells were grown in Essential 8 (made in-house based on (57)) on GelTrex (Life Technologies, A1413202), and were maintained at 37°C under a humidified atmosphere of 5% CO_2 in air. Cells were cultured in the absence of antibiotics and tested for mycoplasma quarterly. DNA of cells from the working bank was analysed for karyotypic abnormalities by low-pass whole genome sequencing. After 10 passages in culture, cells were checked by qPCR for presence of the most common culture-acquired karyotypic abnormalities (1q, 12p, 17q and 20q), as previously described (58,59).

Zebrafish

All zebrafish were maintained in the University of Sheffield Bateson Centre Aquaria at 28°C. *mfn2*$^{hu3528/+}$ zebrafish have been previously described (13). To generate experimental cohorts *mfn2*$^{hu3528/+}$ fish were in-crossed, and *mfn2*$^{hu3528/hu3528}$ fish were identified using PCR-based genotyping (Chapman et al., 2013).

For drug dosing studies zebrafish were housed in 3.5 L tanks from 5 days to 6 months

old at a maximum stocking density of 10 fish per litre. Beginning at 8 days old, ACY-738 / 2% DMSO (treatment) or 2% DMSO (vehicle) were given intermittently. Treatment or vehicle were applied for 3.5 days and then withdrawn for 3.5 days, to reduce the chances of toxicity. For oral dosing, ACY-738 was also formulated in Gelly Belly™ food mix (Florida Aqua Farms) according to a previously described method (60). In preliminary studies, we established that a 3.5 L tank of zebrafish, at a stocking density of 10 fish per litre, would eat at most 16mg of gelly belly diet twice per day. Thus, ACY-738 was formulated at a dose of 0.058% (w/w) in gelly belly and 16 mg of this was fed to each 3.5 L tank twice per day. The vehicle group received gelly belly diet without ACY-738. Swimming endurance was measured using a custom-built swim tunnel apparatus and critical swimming speed (Ucrit) was calculated as previously described (13).

CRISPR/Cas9 genome editing

Guides and repair template were designed to exon 3 of *MFN2* using Horizon CRISPR design tool (https://horizondiscovery.com/products/tools/CRISPR-Targeted-Gene-Designer) (cRNA sequence: TCAGTGAGGTGCTGGCTCGG Repair Template: AAGTGAGAGGCATCAGTGAGGTGCTGGCTCAGAGGCACATGAAAGTGGCTTTTT TTGGCCG). cRNA and ALT-R® CRISPR-Cas9 tracrRNA (IDT, 1072532) were mixed in equimolar concentrations and heated to 95°C for 5 minutes. The MShef11 cells were transfected with HiFi Cas9 Nuclease V3 (IDT), cRNA:tracrRNA complex and repair template using a DigitalBio Microporator (Thermo Fisher Scientific) with the following settings: 1400V, 20ms, 1 pulse. Cells were grown in E8 supplemented with 10µM Y-27632 for 48 h. Cells were then single-cell sorted using the FACS Jazz (BD Biosciences) into GelTrex-coated 96 well plates. After approximately 14 days of growth, a third of the well contents was transferred to the new culture vessel for expansion for cryopreservation. The rest of the sample was taken for DNA analysis. Sanger sequencing was performed to detect clones with the correct genome

editing of *MFN2*. Putative off-target effects were detected in silico using IDT Guide Checker (https://eu.idtdna.com/site/order/designtool/index/CRISPR_SEQUENCE). The top 5 off-target locations (**Supplementary Table 2**) were checked by Sanger sequencing. Four heterozygous edited clones, *MFN2*$^{R94Q/+}$ Het1 (RRID: CVCL_E3QL), *MFN2*$^{R94Q/+}$ Het3.1 (RRID: CVCL_E3QM), *MFN2*$^{R94Q/+}$ Het3.2 (RRID: CVCL_E3QN), and *MFN2*$^{R94Q/+}$ Het4 (RRID: CVCL_E3QP) were derived in independent CRISPR/Cas9 experiments. *MFN2*$^{+/+}$ WT2 clone (RRID: CVCL_E3QK) and MFN2 $^{R94Q/R94Q}$ Hom1 (RRIDL CVCL_ F4CS) was derived from the same targeting/cloning experiment as *MFN2*$^{R94Q/+}$ Het1.

RNA extraction, reverse transcription and quantitative real-time PCR (qPCR)

For qPCR analyses, RNA was extracted using the Norgen Total RNA Purification Plus Kit (Norgen). RNA was reverse transcribed using High-Capacity Reverse Transcriptase (Applied Biosystems, 4368813) according to the manufacturer's instructions. Each 10 µl qPCR reaction contained 1x PowerTrack SYBR Green Master Mix (Thermo Fisher Scientific, 46109), 100 nM of each forward and reverse primers (**Supplementary Table 3**), and 10 ng of RNA. The PCR reaction was run on a QuantStudio 12K Flex Thermocycler (Thermo Fisher Scientific) with the following parameters: 50°C for 2 minutes, 95°C for 10 minutes, then 40 cycles of 95°C for 15 seconds, 60°C for 1 minute. The cycle times were obtained from the QuantStudio 12K Flex Software with auto baseline settings and were then exported to Excel for analysis using the ΔΔCt method.

Immunocytochemistry

Cells were fixed with 4% paraformaldehyde (PFA) for 15 minutes at room temperature. Cells were then blocked and permeabilised with 0.2% Triton X-100 (Sigma) in PBS supplemented with 10% foetal calf serum for 1 hr at room temperature. Primary antibodies (**Supplementary**

573 **Table 4**) were incubated with samples at 4°C overnight. Secondary antibodies
574 (**Supplementary Table 5**) were incubated for 1 hour at room temperature in the dark. Nuclei
575 were counterstained with Hoechst 33342 (Thermo Fisher Scientific). Stained cells were imaged
576 using either the Incell Analyser 2000 (GE Healthcare) or LSM880 AiryScan Confocal (Zeiss).
577 Images were analysed using Cell Profiler (61) using custom-made protocols.
578
579 **Differentiation of hESC to spinal motor neurons**
580 Motor neuron differentiation was optimised based on the protocols published by Maury et al.
581 (32) and Guo et al. (21). HPSCs (3000 cells) were plated on day 0 in 96 well U-bottomed low
582 attachment plates (Greiner) in N2B27 media (DMEM-F12 50:50 mix with Neurobasal (Gibco),
583 N2 (Gibco) 1:100, B27 (Gibco) 1:50, Glutamax (Gibco) 1:100, Non-essential Amino Acids
584 (Gibco) 1:100, beta-mercaptoethanol (Gibco) 1:1000) containing, 20 ng/ml FGF-2 (R&D
585 systems), 5 μM Y-27632 (Generon), 0.2 μM LDN193189 (Tocris), 4 μM Chir99021 (Tocris),
586 40 μM SB431542 (Tocris) and 0.05% PVA (Sigma). Plates were spun at 1400 rpm for 4
587 minutes. 50% media changes were performed every two days unless otherwise stated. At day
588 2, medium was changed to contain 20 ng/ml FGF-2, 0.2 μM LDN193189, 4 μM Chir99021,
589 40 μM SB431542, 1 μM all-*trans* retinoic acid (Sigma) and 0.5 μM SAG (Tocris). At day 4,
590 medium contained 1 μM all-*trans r*etinoic acid and 0.5 μM SAG At day 7 medium contained
591 1μM all-*trans* retinoic acid, 0.5 μM SAG, 10 ng/ml BDNF (Peprotech) and 10 ng/ml GDNF
592 (Peprotech). At day 9, medium was changed to contain 10 μM DAPT (Tocris) 10 ng/ml BDNF,
593 10 ng/ml GDNF, 1 μM all-*trans* retinoic acid and 0.5 μM SAG. At day 13, spheres were pooled
594 together, dissociated using accutase and re-plated on Poly-L-Ornithine (Sigma, P4957) and
595 GelTrex- coated dishes in media containing 10 μM DAPT, 10 ng/ml BDNF, 10 ng/ml GDNF,
596 0.1 μM retinoic acid and 0.5 μM SAG. At day 14, retinoic acid and SAG were removed from
597 the culture media and DAPT was increased to 20 μM. At day 16, 10 ng/ml CNTF (Peprotech)

was added to the culture media. On day 17, DAPT was removed from the media. From this point on media contained only BDNF, GDNF, CNTF at 10 ng/ml. Cells were used for experiments on day 16 or 34 as stated.

HiPSCs were differentiated as previously described (Van Lent et al., 2021) on microfluidic devices (Supplementary Figure 6C).

Differentiation of hESC to enteric neurons

Enteric neuron differention was carried out using a modified version of a previously published protocol (62). Briefly, hESCs were seeded at 40,000 cells/cm 2 on Vitronectin (ThermoFisher)-coated plates in vagal neural crest medium (DMEM-F12 (Gibco), 1:100 GlutaMAX (Gibco), 1:100 MEM-NEAA (Gibco), 1:100 N2-B (Stem Cell Technologies), 1 μM CHIR99021 (Tocris), 10 μM Y-27632 (Generon), 20 ng/ml BMP4 (ThermoFisher), 1 μM SB421542 (Tocris), and 200 nM LDN193189 (Tocris)). Y-27632 was removed from the media on Day 2. All-trans retinoic acid (Sigma) was added to the media on Day 4 and Day 5 at a final concentration of 1 μM. On Day 6, the resulting vagal neural crest cells were replated at 150,000 cells/cm 2 on GelTrex-coated ibidi dishes in enteric nervous system (ENS) induction medium (Neurobasal (Gibco), 1:100 N2-B, 1:100 GlutaMAX, 1:50 B27 (Gibco), 100 μM ascorbic acid (Sigma), 25 ng/ml GDNF (Peprotech), and 10 μM Y-27632). On Day 7, replated cells were fed with ENS induction medium without Y-27632. Cells were fed every day for a further 12 days by 50% media changes.

Time-lapse analysis of mitochondrial movement

Motor neurons (differentiation day 13) were seeded into PLO/GelTrex-coated 35 mm dishes (Ibidi, 81156) and differentiated as detailed above. On day 34 of differentiation, neurons were transfected with a 1:1 ratio of pCAG GFP (63) and DsRed2-Mito (Tanaka Bio) plasmids using

Lipofectamine LTX Plus (Thermo Fisher Scientific, 15338100) for 6 hours, before fresh media replacement. A total of 1 μg of plasmid DNA was added to each 35 mm Ibidi dish. Treatment, if applicable, was added after 24 hours post-transfection. Neurons were imaged 48 hours post-transfection in widefield using a custom imaging system (Cairn Research) at 37°C. This system uses a Ti2-E automated inverted microscope base (Nikon), ASI automated XY & piezo-Z stage controller, iLas 2 scanning TIRF/FRAP unit (Gataca Systems) with dual-collimation optics, Cairn multi-line laserbank, and a Photometrics Prime 95B sCMOS camera. Imaging was performed with a 488 nm and 561 nm laser, a quad-band filter cube (TRF89901-EMv2, Chroma) and additional emission clean up provided by a Cairn Optospin filter wheel with ET525/50m or ET595/44m filters for 488 and 561 laser lines respectively. Images were taken in MetaMorph acquisition software using a Nikon CFI Apochromat Lamda 60X oil (N.A. 1.40, W.D. 0.13 mm) objective lens. For time-lapse imaging, images of DsRed2 were taken every 500 milliseconds for 2.5 minutes, and GFP images were taken in the first and last frames. Recordings were made in the proximal regions (within 500 μm from cell body), mid regions (500 μm to 1500 μm from the cell body), and distal regions (>1500 μm from the cell body) of the neuron. 2-4 neurons per cell line per condition were recorded from each independent differentiation. The first frame of each time-lapse was thresholded and the area and shape descriptors were calculated for mitochondria within the axon of interest. Kymographs were generated from time-lapse images using a custom-made FIJI macro. Kymographs were segmented and run through KymoButler (64) to generate track predictions. Kymograph segments with KymoButler track predictions were restitched in R, and motility and velocity measures were calculated from here (Supplementary Figure 8). After each timelapse, the entire neuron was imaged using GFP to calculate the total length and where each individual recording was in relation to the cell body. Mitochondrial morphology in the axon was calculated by taking the first frame of each kymograph and “Analyse Particles” was run on a thresholded image to

measure individual mitochondria. Instantaneous velocity was calculated by manually adding short (<40 pixel) straight lines to individual discrete movements on kymographs and calculating the distance covered over change in time. Whole track velocity was calculated by taking the total distance covered over change in time of a single motile track. The pause coefficient was determined by calculating how long a track spent paused via a sliding window of 4 seconds and summing this value for all motile tracks in a kymograph, then dividing this by the total distance travelled by all motile tracks in a kymograph to normalise. Velocity variation was calculated using a sliding window of 4 seconds to calculate velocity across a motile track.

Protein extraction

Adherent cells were washed in phosphate buffered saline (PBS, 137 mM NaCl, 2.7 mM KCl, 1.5 mM KH_2PO_4, 10 mM $Na_2PO_4.2H_2O$), scraped into Laemmli buffer (60 mM Tris HCl pH 6.8, 2% SDS, 0.002% bromophenol blue, 5% β-mercaptoethanol, 5% glycerol) and 1x DNase I (Thermo Fisher Scientific). Protein samples were denatured at 100°C for 5 min before analysis by immunoblot.

Endogenous immunoprecipitation

hESCs were washed with cold PBS and harvested into modified Tris buffer (50 mM Tris pH 7.5, 150 nM NaCl, 2 mM EDTA, 5% w/v glycerol, 1% w/v NP-40, 1 x Halt™ Protease and Phosphatase Inhibitor Cocktail (Thermo Fisher Scientific)) and lysed at 4 °C for 30 min. Lysates were cleared by centrifugation at 15,000×*g* for 20 min at 4 °C, and 6 mg protein was incubated with 5 µl α-MFN2 primary antibody (Cell Signalling Technology) overnight at 4°C. 40 µl Protein A Mag Sepharose beads (GE Healthcare) were added to the samples and incubated for 3 h at 4°C. Beads were washed with buffer and eluted for downstream experiments. with 30 µl 5% SDS/50 mM Tris, pH 7.4 and heating at 70 °C for 15 minutes.

672

673 **Mass spectrometry analysis of MFN2 immunoprecipitations**

674 25 µl of IP elutions (5% SDS/50 mM Tris, pH 7.4), were reduced with TCEP to a final
675 concentration of 5 mM and heated at 70 °C for 15 minutes. Proteins were alkylated by adding
676 Iodoacetamide (IAA) to a final concentration of 10 mM, and the samples were incubated at 37
677 °C in the dark for 30 minutes. 2.5 µl of 12 % phosphoric acid and 165 µl of S-Trap binding
678 buffer (90% methanol, 100 mM TEAB, pH 7.1) were then added to each sample. Samples were
679 then loaded into S-Trap columns (ProtiFi) by centrifugation at 10,000 x g for 60 seconds.
680 Samples were washed four times with 225 µl of S-Trap binding buffer through centrifugation
681 at 10,000 x g for 60 seconds. 1 µg of Trypsin (Pierce, sequencing grade) was added to each
682 sample in a total digestion volume of 20 µl of 50 mM TEAB, and digestion was performed at
683 47 °C for 1 hour, followed by 37 °C for 1 hour. Peptides were eluted with the addition of 40 µl
684 of 50 mM TEAB, 40 µl of 0.2% aqueous formic acid, and then 40 µl of 50% acetonitrile with
685 0.2% formic acid, followed by centrifugation at 10,000 x g for 60 seconds for each elution.
686 Pooled eluted peptides were dried in a vacuum concentrator and resuspended in 0.5% formic
687 acid for LC-MS/MS analysis. Each sample was analysed using nanoflow LC-MS/MS using an
688 Orbitrap Exploris 480 (Thermo Fisher) mass spectrometer equipped with an EASY-Spray
689 source coupled to a Vanquish LC System (Thermo Fisher). Peptides were desalted online using
690 a Pepmap Neo C18 nano trap column, 300 µm I.D. x 5 mm (Thermo Fisher) and then separated
691 using an EASY-Spray column, 50 cm × 75 µm ID, PepMap Neo C18, 2 µm particles, 10 Å
692 pore size (Thermo Fisher) and separated using a 70-minute gradient. The Orbitrap Exploris 480
693 was operated in positive mode using a Velocity DIA method. MS1 spectra were acquired at a
694 resolution of 60,000 at m/z 200 with a normalised AGC target of 300%. For the DIA analysis,
695 multiply charged precursors in 40 m/z bins (400-900 mz range) were accumulated with a

normalised AGC target of 800%, subjected to HCD fragmentation (145-1500 m/z) with a collision energy of 30%.

Raw mass spectrometry data files were processed with DIA-NN version 2.3.0. Data were analysed in library-free mode using a peptide library predicted from a Human proteome Fasta file (downloaded Aug 2025) containing 20475 proteins. The following settings were used in library prediction. Trypsin was set as the protease, with a maximum of 1 missed cleavage. Cysteine carbamidomethylation was enabled as a fixed modification. Maximum number of variable modifications set to 1 and acetyl-protein N term set as a variable modification. An FDR of 1% used for identification-level cut-offs. The DIA-NN output was loaded into Perseus version 1.6.10.50, and the matrix was filtered to remove all proteins that were potential contaminants and decoy hits. LFQ intensities were log2(x)- transformed, and data were filtered to retain proteins with a minimum of two peptides and at least 3 valid LFQ intensities in one group. Data were normalised by subtracting column medians, and missing values were imputed from the normal distribution with a width of 0.3 and downshift of 1.8. To identify quantitatively enriched proteins in MFN2 IPs versus control IPs, two-sided Student's t-tests were performed with a permutation-based FDR of 0.05. To identify differences in MFN2 interactions between variant and wild type, only proteins significantly enriched in IP versus controls were considered. LFQ intensities were instead normalised to the bait protein, and missing values were imputed from the normal distribution with a width of 0.3 and downshift of 1.8, and two-sided Student's t-tests were performed with a permutation-based FDR of 0.05.

Western blotting

Proteins were separated by SDS–PAGE and transferred to nitrocellulose membranes (Whatman, Fisher Scientific) by electroblotting (Bio-Rad). After transfer, membranes were

blocked for 1 h at room temperature in Tris-buffered saline (TBS) with 5% fat-free milk and 0.1% Tween-20. Membranes were incubated with primary antibodies in blocking buffer overnight at 4°C. Membranes were washed 3 times for 5 min in TBS with 0.1% Tween-20 before incubation with near-infrared AlexaFluor-coupled secondary antibodies in TBS with 0.1% Tween-20 for 1 h at room temperature. Membranes were washed 3 times for 5 min in TBS with 0.1% Tween-20 before near-infrared fluorescent signals were detected using an Odyssey XF Imaging System with ImageStudio software (LI-COR Biosciences UK Ltd, Cambridge, UK). For primary and secondary antibodies used in immunoblotting, see **Supplementary Tables 6 and 7.**

Electrophysiology

Whole-cell patch clamp was used to record membrane currents or membrane potentials from single cells (n = 33), at room temperature (20-25°C), using an Optopatch (Cairn Research Ltd, UK) patch clamp amplifier. The extracellular solution contained (mM): 135 NaCl, 5.8 KCl, 1.3 $CaCl_2$, 0.9 $MgCl_2$, 0.7 NaH_2PO_4, 5.6 D-glucose, 10 Hepes-NaOH, 2 sodium pyruvate. Amino acids and vitamins for Eagle's minimal essential medium (MEM) were added from concentrates (Invitrogen, UK). The pH was adjusted to 7.5 and the osmolality was around 308 mosmol kg^{-1}. Cells were viewed using an upright microscope equipped with Nomarski DIC optics (Nikon FN1, Japan) and were continuously perfused with extracellular solution. Patch electrodes were pulled from soda glass capillaries (Hilgenberg GmbH, Germany) and electrodes had resistances in extracellular solution of around 4 MΩ. The shank of the electrode was coated with surf wax (Mr Zogs Sexwax, USA) to minimise the fast electrode capacitive transients. The pipette solution contained (mM): 131 KCl, 3 $MgCl_2$, 1 EGTA-KOH, 5 Na_2ATP, 5 Hepes-KOH, 10 sodium phosphocreatine (pH 7.3, 290 mosmol kg^{-1}). Voltage and current clamp protocol application and data acquisition were performed using pClamp software and a

Digidata 1440A (Molecular Devices, USA). Recordings were filtered at 2.5 or 10 kHz (8-pole Bessel), sampled at 5 or 100 kHz and stored on computer for off-line analysis using Clampfit, GraphPad Prism (GraphPad Software Inc, USA) and Origin (OriginLab, USA) software. Recordings and reported currents and conductances were corrected off-line for the linear leak conductance. Membrane potentials under voltage clamp were corrected for the voltage drop across the residual series resistance (R_s) at steady-state current level and for a liquid junction potential, measured between pipette and bath solutions, of –4 mV.

Statistical analysis

Statistical analysis was performed using Graphpad Prism version 9.3.1 or R by statistical tests as indicated in figure legends. Data was tested for normality via a Shapiro-Wilks test and distribution observations, and descriptive statistics were determined to examine the SD for each sample. If data was found to be normally distributed, then a Student's t Test or ANOVA with Dunnett's T3 multiple comparisons test was used. If data was found to not be normally distributed, a Mann-Whitney U test or a Kruskal-Wallis test with Dunn's multiple comparisons was performed. For all the statistical tests $p<0.05$ was used as the criterion for statistical significance.

Study approval

Zebrafish experiments were conducted according to UK law under project license 40/8309 granted to AJG, and were subject to a local ethical review process.

Data and code availability

Code that was used to analyse Kymobutler outputs is deposited in ORDA, the University of Sheffield data repository, powered by Figshare.

The mass spectrometry proteomics data have been deposited to the ProteomeXchange Consortium via the PRIDE partner repository with the dataset identifier PXD077751.

Data points used to create figures are availale in the Supporting Data Values file.

Funding Support

This work was partly supported by: Muscular Dystrophy UK 22GRO-PG24-0571-1, the Medical Research Council (MRC) (MR/X000028/1, MR/X007979/1, MR/X012220/1), Hereditary Neuropathy Foundation and an MRC DiMeN studentship. A.E.T is a Sir Henry Dale Fellow, funded by the Wellcome Trust and the Royal Society (220192/Z/20/Z). This work was also supported in part by the University of Antwerp (DOC-PRO4 PhD fellowship to J.V.L., TOP-BOF research grant N_38694 to V.T.). V.T. is a member of the μNeuro Center of Excellence at the University of Antwerp. K.J.D.V was supported by MRC (MR/S025979/1), Alzheimer's Society (AS-PG-15-023), and Alzheimer's Research UK (ARUK-PG2019A-008) project grants.

Author contributions

L.H.J, LB, R.A.L, K.I.A, J.V.L, S.L.J, H.W, B.A, E.B, O.L, C.J.P, E.D, M.O.C, and D.S conducted experiments and acquired data. K.D.V and I.B provided reagents. L.H.J, L.B, K.I.A, J.V.L, S.L.J, B.A, A.T, M.O.C, V.T, K.J.D.V, A.T, A.J.G, and I.B designed research studies and analysed data. L.H.J, L.B, A.J.G, and I.B wrote and edited the manuscript. J.V.L, B.A, O.L, G.G, A.T, V.T, K.J.D.V, A.T, and A.J.G edited the manuscript.

Bibliography

1. Reilly MM, Murphy SM, Laura M. Charcot-Marie-Tooth disease. *J Peripher Nerv Syst*. Mar 2011;16(1):1–14.
2. Pipis M, Feely SME, Polke JM, et al. Natural history of Charcot-Marie-Tooth disease type 2A: a large international multicentre study. *Brain*. Dec 1 2020;143(12):3589–3602.
3. Feely SM, Laura M, Siskind CE, et al. MFN2 mutations cause severe phenotypes in most patients with CMT2A. *Neurology*. May 17 2011;76(20):1690–6.
4. Zuchner S, Mersiyanova IV, Muglia M, et al. Mutations in the mitochondrial GTPase mitofusin 2 cause Charcot-Marie-Tooth neuropathy type 2A. *Nat Genet*. May 2004;36(5):449–51.
5. Chandhok G, Lazarou M, Neumann B. Structure, function, and regulation of mitofusin-2 in health and disease. *Biol Rev Camb Philos Soc*. May 2018;93(2):933–949.
6. Stuppia G, Rizzo F, Riboldi G, et al. MFN2-related neuropathies: Clinical features, molecular pathogenesis and therapeutic perspectives. *J Neurol Sci*. Sep 15 2015;356(1-2):7–18.
7. Verhoeven K, Claeys KG, Zuchner S, et al. MFN2 mutation distribution and genotype/phenotype correlation in Charcot-Marie-Tooth type 2. *Brain*. Aug 2006;129(Pt 8):2093–102.
8. Abati E, Manini A, Velardo D, et al. Clinical and genetic features of a cohort of patients with MFN2-related neuropathy. *Sci Rep*. Apr 13 2022;12(1):6181.
9. Ando M, Hashiguchi A, Okamoto Y, et al. Clinical and genetic diversities of Charcot-Marie-Tooth disease with MFN2 mutations in a large case study. *J Peripher Nerv Syst*. Sep 2017;22(3):191–199.
10. Dorn GW, 2nd. Mitofusin 2 Dysfunction and Disease in Mice and Men. *Front Physiol*. 2020;11:782.
11. Prior R, Van Helleputte L, Benoy V, et al. Defective axonal transport: A common pathological mechanism in inherited and acquired peripheral neuropathies. *Neurobiol Dis*. Sep 2017;105:300–320.
12. Baloh RH, Schmidt RE, Pestronk A, et al. Altered axonal mitochondrial transport in the pathogenesis of Charcot-Marie-Tooth disease from mitofusin 2 mutations. *J Neurosci*. Jan 10 2007;27(2):422–30.
13. Chapman AL, Bennett EJ, Ramesh TM, et al. Axonal Transport Defects in a Mitofusin 2 Loss of Function Model of Charcot-Marie-Tooth Disease in Zebrafish. *PLoS One*. 2013;8(6):e67276.
14. Rocha AG, Franco A, Krezel AM, et al. MFN2 agonists reverse mitochondrial defects in preclinical models of Charcot-Marie-Tooth disease type 2A. *Science*. Apr 20 2018;360(6386):336–341.
15. Rossaert E, Van Den Bosch L. HDAC6 inhibitors: Translating genetic and molecular insights into a therapy for axonal CMT. *Brain Res*. Apr 15 2020;1733:146692.
16. Picci C, Wong VSC, Costa CJ, et al. HDAC6 inhibition promotes alpha-tubulin acetylation and ameliorates CMT2A peripheral neuropathy in mice. *Exp Neurol*. Jun 2020;328:113281.
17. Shen S, Picci C, Ustinova K, et al. Tetrahydroquinoline-Capped Histone Deacetylase 6 Inhibitor SW-101 Ameliorates Pathological Phenotypes in a Charcot-Marie-Tooth Type 2A Mouse Model. *J Med Chem*. Apr 22 2021;64(8):4810–4840.
18. d'Ydewalle C, Krishnan J, Chiheb DM, et al. HDAC6 inhibitors reverse axonal loss in a mouse model of mutant HSPB1-induced Charcot-Marie-Tooth disease. *Nat Med*. Jul 24 2011;17(8):968–74.
19. Benoy V, Van Helleputte L, Prior R, et al. HDAC6 is a therapeutic target in mutant GARS-induced Charcot-Marie-Tooth disease. *Brain*. Mar 1 2018;141(3):673–687.

20. Fazal R, Boeynaems S, Swijsen A, et al. HDAC6 inhibition restores TDP-43 pathology and axonal transport defects in human motor neurons with TARDBP mutations. *EMBO J*. Apr 1 2021;40(7):e106177.
21. Guo W, Naujock M, Fumagalli L, et al. HDAC6 inhibition reverses axonal transport defects in motor neurons derived from FUS-ALS patients. *Nat Commun*. Oct 11 2017;8(1):861.
22. Davis-Dusenbery BN, Williams LA, Klim JR, et al. How to make spinal motor neurons. *Development*. Feb 2014;141(3):491–501.
23. Nedelec S, Martinez-Arias A. In vitro models of spinal motor circuit's development in mammals: achievements and challenges. *Curr Opin Neurobiol*. Feb 2021;66:240–249.
24. Thomson JA, Itskovitz-Eldor J, Shapiro SS, et al. Embryonic stem cell lines derived from human blastocysts. *Science*. Nov 6 1998;282(5391):1145–7.
25. Takahashi K, Tanabe K, Ohnuki M, et al. Induction of pluripotent stem cells from adult human fibroblasts by defined factors. *Cell*. Nov 30 2007;131(5):861–72.
26. Thompson O, von Meyenn F, Hewitt Z, et al. Low rates of mutation in clinical grade human pluripotent stem cells under different culture conditions. *Nat Commun*. Mar 23 2020;11(1):1528.
27. Stifani N. Motor neurons and the generation of spinal motor neuron diversity. *Front Cell Neurosci*. 2014;8:293.
28. Nakano T, Windrem M, Zappavigna V, et al. Identification of a conserved 125 base-pair Hb9 enhancer that specifies gene expression to spinal motor neurons. *Dev Biol*. Jul 15 2005;283(2):474–85.
29. Mizuguchi R, Sugimori M, Takebayashi H, et al. Combinatorial roles of olig2 and neurogenin2 in the coordinated induction of pan-neuronal and subtype-specific properties of motoneurons. *Neuron*. Sep 13 2001;31(5):757–71.
30. Rayon T, Maizels RJ, Barrington C, et al. Single-cell transcriptome profiling of the human developing spinal cord reveals a conserved genetic programme with human-specific features. *Development*. Aug 1 2021;148(15)
31. Dasen JS, Jessell TM. Hox networks and the origins of motor neuron diversity. *Curr Top Dev Biol*. 2009;88:169–200.
32. Maury Y, Come J, Piskorowski RA, et al. Combinatorial analysis of developmental cues efficiently converts human pluripotent stem cells into multiple neuronal subtypes. *Nat Biotechnol*. Jan 2015;33(1):89–96.
33. Van Lent J, Verstraelen P, Asselbergh B, et al. Induced pluripotent stem cell-derived motor neurons of CMT type 2 patients reveal progressive mitochondrial dysfunction. *Brain*. Sep 4 2021;144(8):2471–2485.
34. Mou Y, Dein J, Chen Z, et al. MFN2 Deficiency Impairs Mitochondrial Transport and Downregulates Motor Protein Expression in Human Spinal Motor Neurons. *Front Mol Neurosci*. 2021;14:727552.
35. De Vos KJ, Sheetz MP. Visualization and quantification of mitochondrial dynamics in living animal cells. *Methods Cell Biol*. 2007;80:627–82.
36. Gogolou A, Frith TJR, Tsakiridis A. Generating Enteric Nervous System Progenitors from Human Pluripotent Stem Cells. *Curr Protoc*. Jun 2021;1(6):e137.
37. Frith TJR, Gogolou A, Hackland JOS, et al. Retinoic Acid Accelerates the Specification of Enteric Neural Progenitors from In-Vitro-Derived Neural Crest. *Stem Cell Reports*. Sep 8 2020;15(3):557–565.
38. Oughtred R, Rust J, Chang C, et al. The BioGRID database: A comprehensive biomedical resource of curated protein, genetic, and chemical interactions. *Protein Sci*. Jan 2021;30(1):187–200.

898 39. Sugiura A, Nagashima S, Tokuyama T, et al. MITOL regulates endoplasmic
899 reticulum-mitochondria contacts via Mitofusin2. *Mol Cell*. Jul 11 2013;51(1):20–34.
900 40. Komatsu M, Waguri S, Ueno T, et al. Impairment of starvation-induced and
901 constitutive autophagy in Atg7-deficient mice. *J Cell Biol*. May 9 2005;169(3):425–34.
902 41. Komatsu M, Wang QJ, Holstein GR, et al. Essential role for autophagy protein Atg7
903 in the maintenance of axonal homeostasis and the prevention of axonal degeneration. *Proc
904 Natl Acad Sci U S A*. Sep 4 2007;104(36):14489–94.
905 42. Murakawa T, Yamaguchi O, Hashimoto A, et al. Bcl-2-like protein 13 is a
906 mammalian Atg32 homologue that mediates mitophagy and mitochondrial fragmentation.
907 *Nat Commun*. Jul 6 2015;6:7527.
908 43. Klinman E, Holzbaur EL. Stress-Induced CDK5 Activation Disrupts Axonal
909 Transport via Lis1/Ndel1/Dynein. *Cell Rep*. Jul 21 2015;12(3):462–73.
910 44. Pandey JP, Smith DS. A Cdk5-dependent switch regulates Lis1/Ndel1/dynein-driven
911 organelle transport in adult axons. *J Neurosci*. Nov 23 2011;31(47):17207–19.
912 45. Nourbakhsh K, Ferreccio AA, Bernard MJ, et al. TAOK2 is an ER-localized kinase
913 that catalyzes the dynamic tethering of ER to microtubules. *Dev Cell*. Dec 20
914 2021;56(24):3321–3333 e5.
915 46. Baffet AD, Benoit B, Januschke J, et al. Drosophila tubulin-binding cofactor B is
916 required for microtubule network formation and for cell polarity. *Mol Biol Cell*. Sep
917 2012;23(18):3591–601.
918 47. Dompierre JP, Godin JD, Charrin BC, et al. Histone deacetylase 6 inhibition
919 compensates for the transport deficit in Huntington's disease by increasing tubulin
920 acetylation. *J Neurosci*. Mar 28 2007;27(13):3571–83.
921 48. Jochems J, Teegarden SL, Chen Y, et al. Enhancement of stress resilience through
922 histone deacetylase 6-mediated regulation of glucocorticoid receptor chaperone dynamics.
923 *Biol Psychiatry*. Feb 15 2015;77(4):345–55.
924 49. Outeiro TF, Kontopoulos E, Altmann SM, et al. Sirtuin 2 inhibitors rescue alpha-
925 synuclein-mediated toxicity in models of Parkinson's disease. *Science*. Jul 27
926 2007;317(5837):516–9.
927 50. Wang X, Schwarz TL. The Mechanism of Ca2+-Dependent Regulation of Kinesin-
928 Mediated Mitochondrial Motility. *Cell*. 2009/01/09/ 2009;136(1):163–174.
929 51. Liang WH, Li Q, Rifat Faysal KM, et al. Microtubule Defects Influence Kinesin-
930 Based Transport In Vitro. *Biophys J*. May 24 2016;110(10):2229–40.
931 52. Guillaud L, Wong R, Hirokawa N. Disruption of KIF17-Mint1 interaction by
932 CaMKII-dependent phosphorylation: a molecular model of kinesin-cargo release. *Nat Cell
933 Biol*. Jan 2008;10(1):19–29.
934 53. Hirokawa N, Noda Y, Tanaka Y, et al. Kinesin superfamily motor proteins and
935 intracellular transport. *Nat Rev Mol Cell Biol*. Oct 2009;10(10):682–96.
936 54. Guedes-Dias P, Nirschl JJ, Abreu N, et al. Kinesin-3 Responds to Local Microtubule
937 Dynamics to Target Synaptic Cargo Delivery to the Presynapse. *Curr Biol*. Jan 21
938 2019;29(2):268–282 e8.
939 55. Mo Z, Zhao X, Liu H, et al. Aberrant GlyRS-HDAC6 interaction linked to axonal
940 transport deficits in Charcot-Marie-Tooth neuropathy. *Nat Commun*. Mar 8 2018;9(1):1007.
941 56. Kumar A, Larrea D, Pero ME, et al. MFN2 coordinates mitochondria motility with
942 alpha-tubulin acetylation and this regulation is disrupted in CMT2A. *iScience*. Jun 21
943 2024;27(6):109994.
944 57. Chen G, Gulbranson DR, Hou Z, et al. Chemically defined conditions for human
945 iPSC derivation and culture. *Nat Methods*. May 2011;8(5):424–9.
946 58. Baker D, Hirst AJ, Gokhale PJ, et al. Detecting Genetic Mosaicism in Cultures of
947 Human Pluripotent Stem Cells. *Stem Cell Reports*. Nov 8 2016;7(5):998–1012.

59. Laing O, Halliwell J, Barbaric I. Rapid PCR Assay for Detecting Common Genetic Variants Arising in Human Pluripotent Stem Cell Cultures. *Curr Protoc Stem Cell Biol*. Jun 2019;49(1):e83.
60. Benjamin JT, Tyler A. A Gelatin-based Diet for Oral Dosing Juvenile to Adult Zebrafish (Danio rerio). 2014:
61. Carpenter AE, Jones TR, Lamprecht MR, et al. CellProfiler: image analysis software for identifying and quantifying cell phenotypes. *Genome Biol*. 2006;7(10):R100.
62. Gogolou A, Frith TJR, Tsakiridis A. Generating Enteric Nervous System Progenitors from Human Pluripotent Stem Cells. *Current Protocols*. 2021–06–01 2021;1(6)
63. Liew CG, Draper JS, Walsh J, et al. Transient and stable transgene expression in human embryonic stem cells. *Stem Cells*. Jun 2007;25(6):1521–8.
64. Jakobs MAH, Dimitracopoulos A, Franze K. KymoButler, a deep learning software for automated kymograph analysis. *Elife*. Aug 13 2019;8

Figures

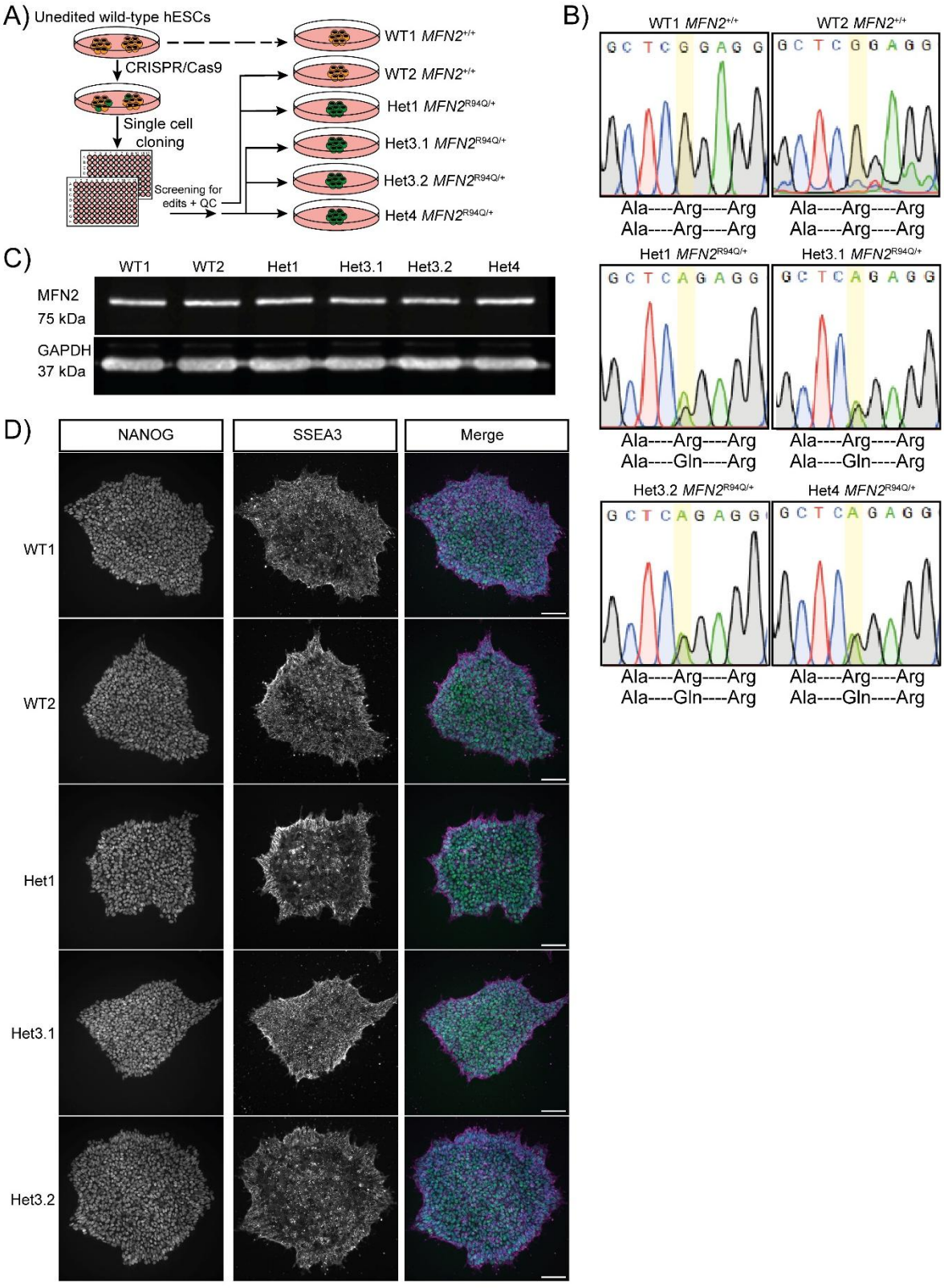

Figure 1: Generation of isogenic *MFN2*$^{R94Q/+}$ and *MFN2*$^{+/+}$ hESC clones using CRISPR/Cas9. (**A**) Schematic depicting workflow for the genome editing and cloning of edited and control sublines. Two separate arrows for clone generation indicates two separate

977 CRISPR experiments. (**B**) DNA sequence analysis verified successful genome editing, with
978 two peaks in the *MFN2*$^{R94Q/+}$ clones (G and A, highlighted in yellow in the sequence) indicating
979 heterozygous editing. Predicted amino acid sequence is shown below the sequence traces, with
980 codon 94 in the center. (**C**) Western blot analysis of MFN2 expression in successfully edited
981 clones. (**D**) Representative images of *MFN2*$^{R94Q/+}$ and *MFN2*$^{+/+}$ hESC stained for NANOG
982 (green) and SSEA3 (magenta) as markers of undifferentiated hESC state. Nuclei are
983 counterstained with Hoechst 33342. Scale bar = 100µm.

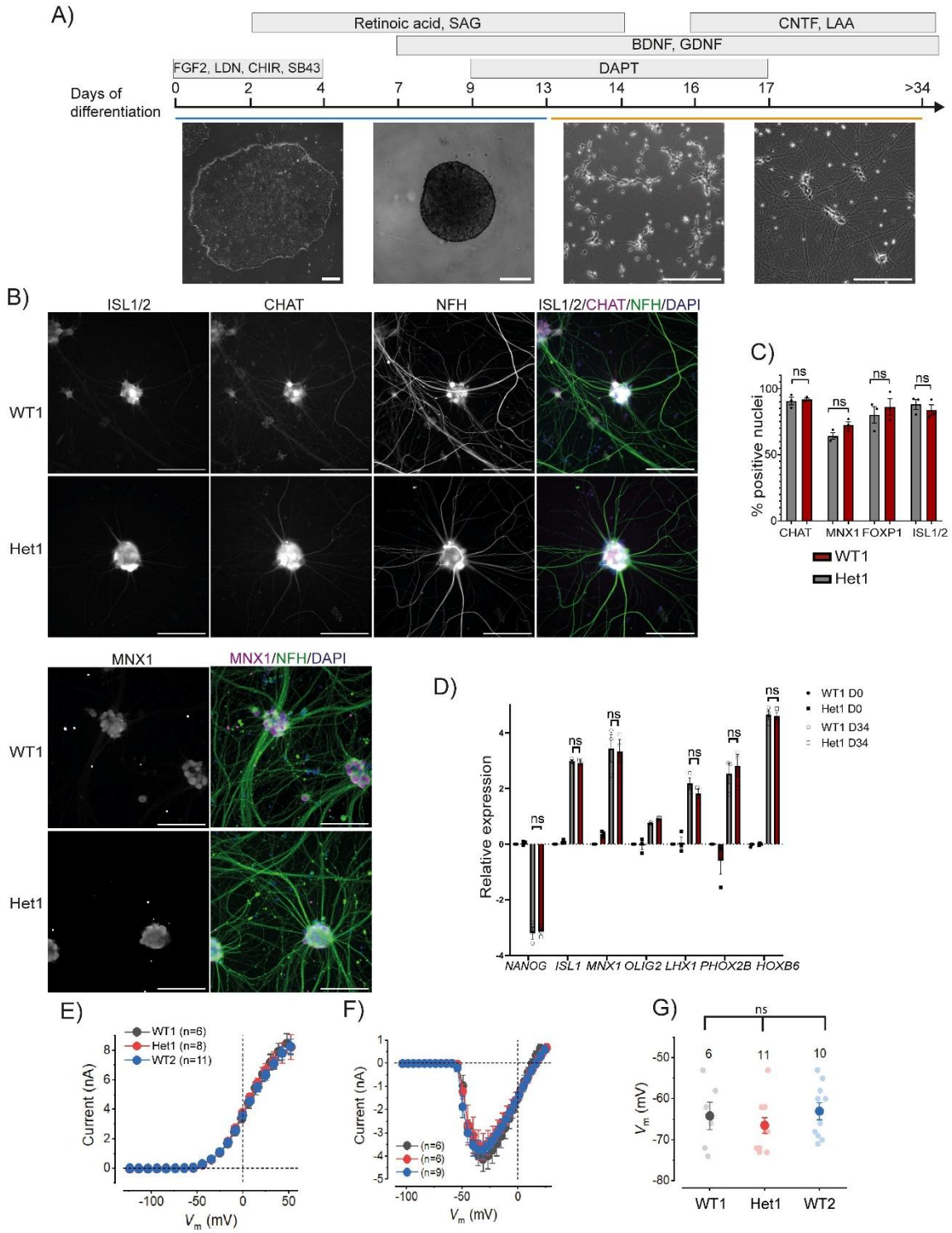

Figure 2: Generation of limb-innervating motor neurons from isogenic *MFN2*$^{R94Q/+}$ and *MFN2*$^{+/+}$ hESC clones. (**A**) Schematic depicting the differentiation protocol for the generation of spinal motor neurons from hESCs. Blue line depicts the 3D portion of the differentiation and the orange line the 2D portion. Scale bar = 100 µm. (**B**) Immunofluorescent analysis of

motor neuron marker expression at Day 34 of differentiation. Scale bar = 100 μm. (**C**) Quantification of immunocytochemistry for motor neuron markers (CHAT, MNX1 (HB9), FOXP1 and ISL1) at day 34 of differentiation. (**D**) Gene expression profiling by qPCR for Day 34 differentiated cells, demonstrating further expression of relevant motor neuron markers (*ISL1, MNX1 (HB9), OLIG2*), columnar markers (*LHX1, PHOX2B*), and HOX markers (*HOXB6*). Data shown is the mean ± SEM of three biological repeats. **p<0.01, ***p<0.001, ****p<0.0001, ns not significant p>0.05, Wilcoxon rank sum test. (**E**) Average steady-state current-voltage (*I-V*) curves for I_K from all WT1 (black), Het1 (red) and WT2 (blue) neurons measured towards the end of the protocol shown in Supplementary Figure 5B. (**F**) Average peak *I-V* curves for I_{Na} from all WT1 (black), Het1 (red) and WT2 (blue) neurons measured at the peak of the inward currents shown in Supplementary Figure 5C, to isolate I_{Na}. (**G**) Resting membrane potentials of WT1 (black), Het1 (red) and WT2 (blue) neurons measured in current clamp at 0pA (from Supplementary Figure 5A).

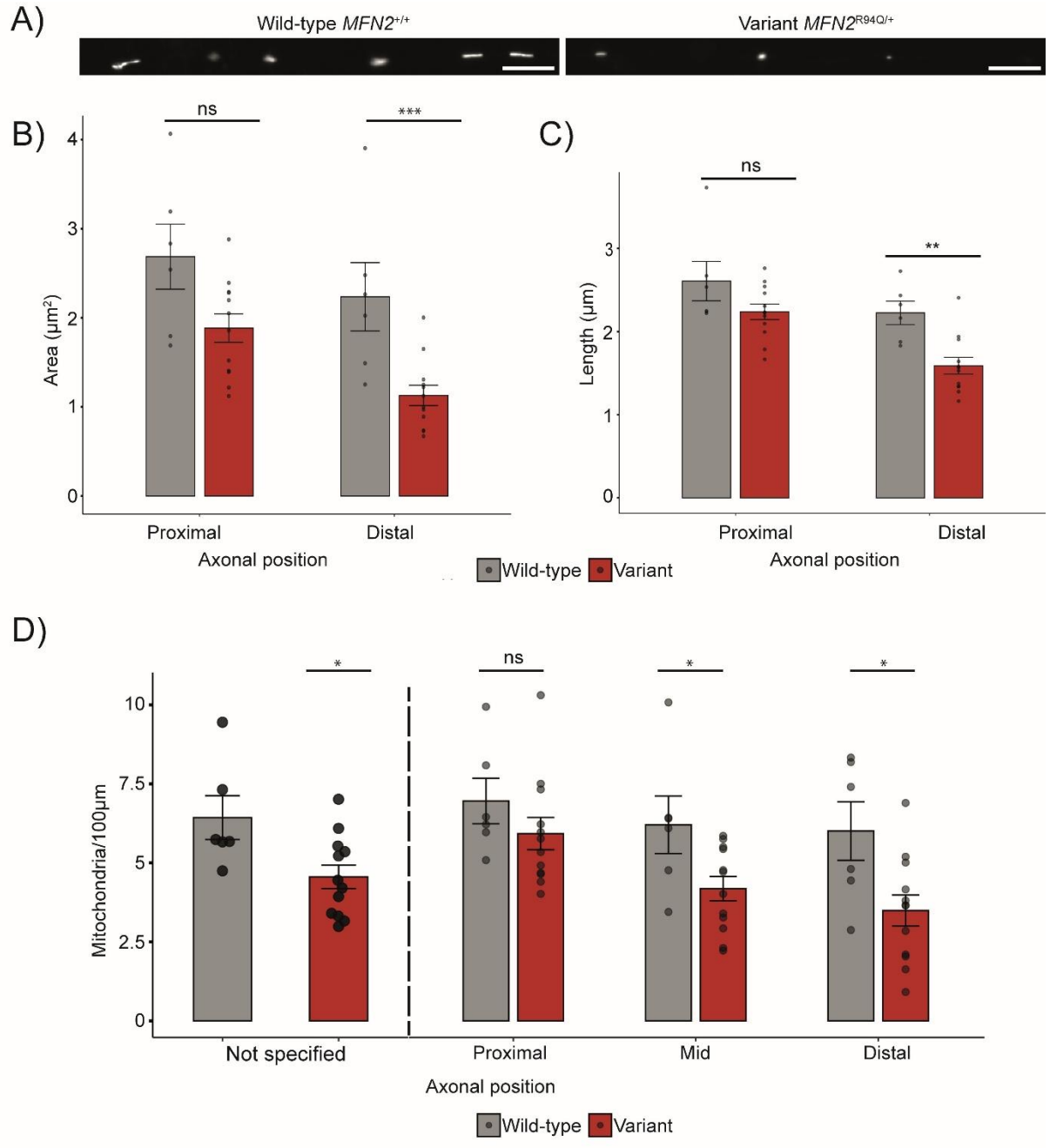

Figure 3: *MFN2*$^{R94Q/+}$ disrupts mitochondrial distribution. (**A**) Representative images of Mito-DsRed2-tagged mitochondria in wild-type and variant axons after 36 days of differentiation. Scale bar = 10 µm. (**B**) Average area of mitochondria in wild-type and variant *MFN2*$^{R94Q/+}$ hESC-derived motor neurons (Day 36). Proximal regions were defined as within 500 µm from cell body, mid regions were 500 µm to 1500 µm from the cell body, and distal regions were >1500 µm from the cell body of the neuron. (**C**) Average length of mitochondria in wild-type and variant *MFN2*$^{R94Q/+}$ hESC-derived motor neurons (Day 36) (**D**) Number of mitochondria per 100 µm averaged across the entire axon, and at proximal, mid, and distal

axonal locations Data shown as mean ± SEM with points representing average values from individual neurons. Statistical significance was calculated with a Wilcoxon rank sum test (N = 6 wild-type, 12 variant) (*P<0.05; **P<0.01; ***P<0.001; ns, not significant).

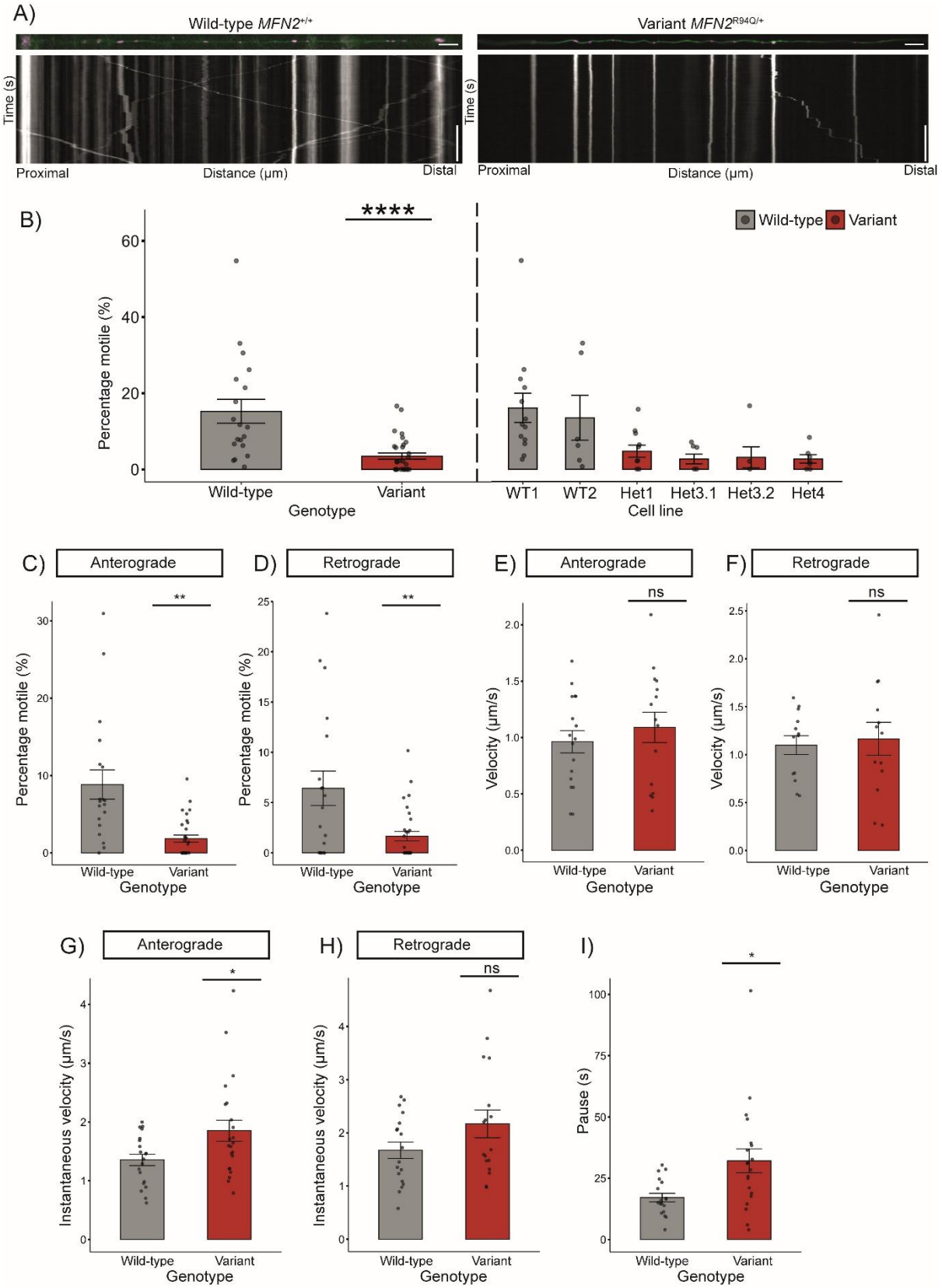

Figure 4: *MFN2*$^{R94Q/+}$ reduces mitochondrial trafficking. (**A**) Representative axons and corresponding kymographs of wild-type and variant neurons after 36 days of differentiation.

Stationary mitochondria are visible as straight lines on kymographs. Mitochondria in motion are shown as diagonal lines. Horizontal scale bar = 10 μm, vertical scale bar = 100 seconds. (**B**) The percentage of motile mitochondria in control and variant lines (Day 36). (**C**) Breakdown of mitochondrial movement into anterograde and (**D**) retrograde movement (Day 36). (**E**) Average whole track velocity of anterograde tracks and (**F**) retrograde tracks (Day 36). (**G**) Instantaneous velocity of anterograde and (**H**) retrograde tracks (Day 36). (**I**) Average length of motile track pauses measured in seconds (Day 36). Data shown as mean ± SEM with points representing average values from individual neurons. Statistical significance was calculated with a Wilcoxon rank sum test (B to I), N = 6 wild-type, 12 variant from 3 independent differentiations (*P<0.05; **P<0.01; ***P<0.001; ****P<0.0001; ns, not significant).

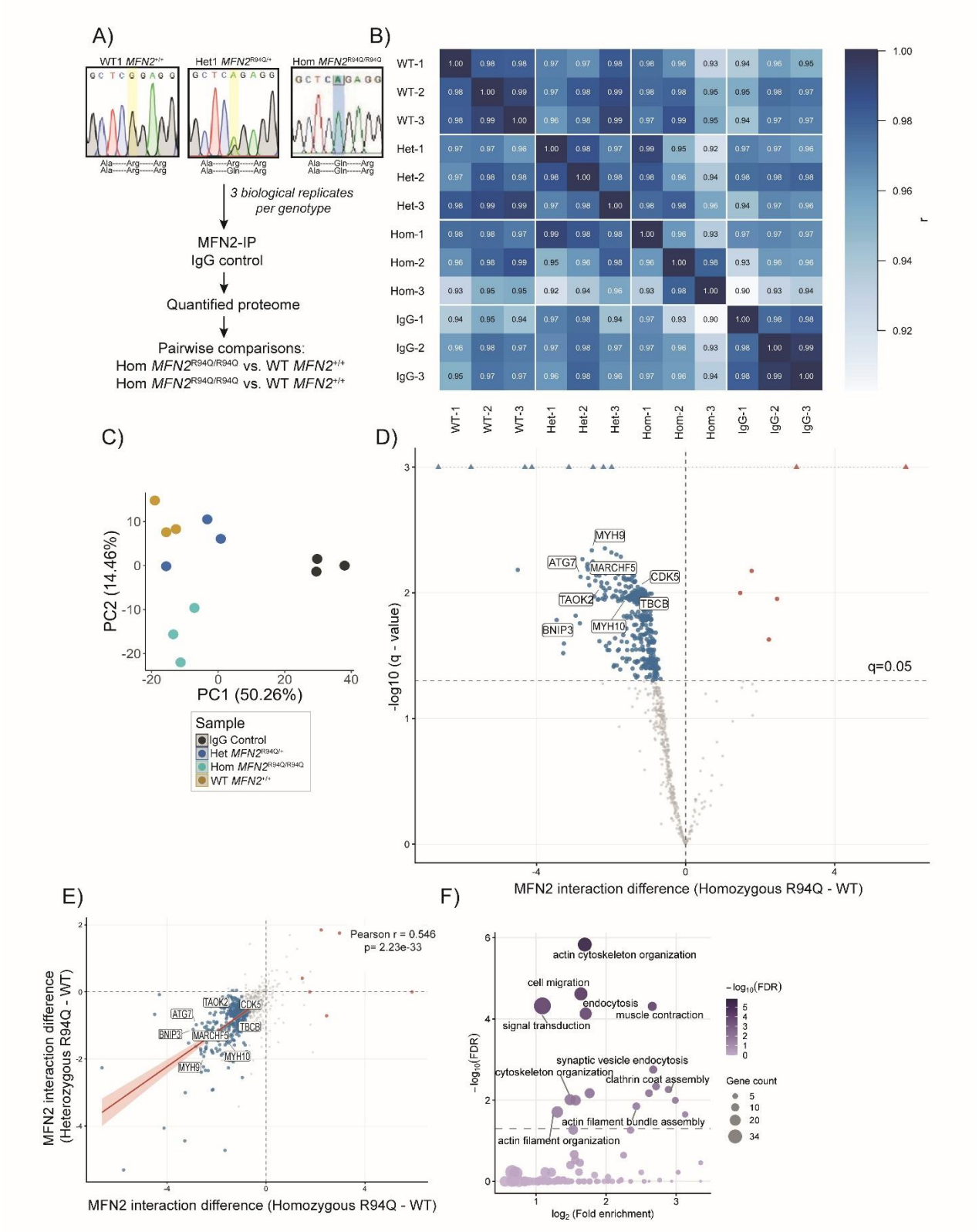

Figure 5. Quantitative mass spectrometry identifies dose-dependent disruption of the MFN2 interactome by R94Q. (**A**) Schematic of the experimental workflow. Endogenous MFN2 was immunoprecipitated from three isogenic hESC lines. IgG immunoprecipitation was

used as a control. Three biological replicates per genotype were analysed by DIA-MS. (**B**) Pearson correlation matrix of log_2-transformed protein intensities across all biological replicates demonstrates reproducibility of the mass spectrometry workflow. (**C**) Principal component analysis of samples, coloured by condition and genotype. Each data point represents one biological replicate (n=3 per condition). (**D**) Bait-corrected volcano plot of *MFN2*$^{R94Q/R94Q}$ versus *MFN2*$^{+/+}$ MFN2 immunoprecipitations. Selected candidates referenced in the text are labelled. (**E**) Dose-dependent reduction of MFN2 partners across the isogenic allele series. Scatter plot of bait-corrected log_2 fold-change (versus *MFN2*$^{+/+}$) for each protein in *MFN2*$^{R94Q/+}$ cells and *MFN2*$^{R94Q/R94Q}$ cells. The 412 candidates significantly reduced in *MFN2*$^{R94Q/R94Q}$ are highlighted in blue and selected candidates referenced in the text are labelled. (**F**) Gene Ontology enrichment analysis of proteins with reduced MFN2 association in MFN2$^{R94Q/R94Q}$ hESCs. Bubble plot showing significantly enriched Biological Process terms for the 412 proteins with significantly reduced MFN2 association in MFN2$^{R94Q/R94Q}$ relative to MFN2$^{+/+}$. Enrichment analysis was performed using DAVID, with all detected proteins (4,299) as a background. Bubble size corresponds to the number of proteins per term; colour indicates the -log10 Benjamini-corrected FDR. Only terms with Benjamini-corrected FDR <0.05 are shown.

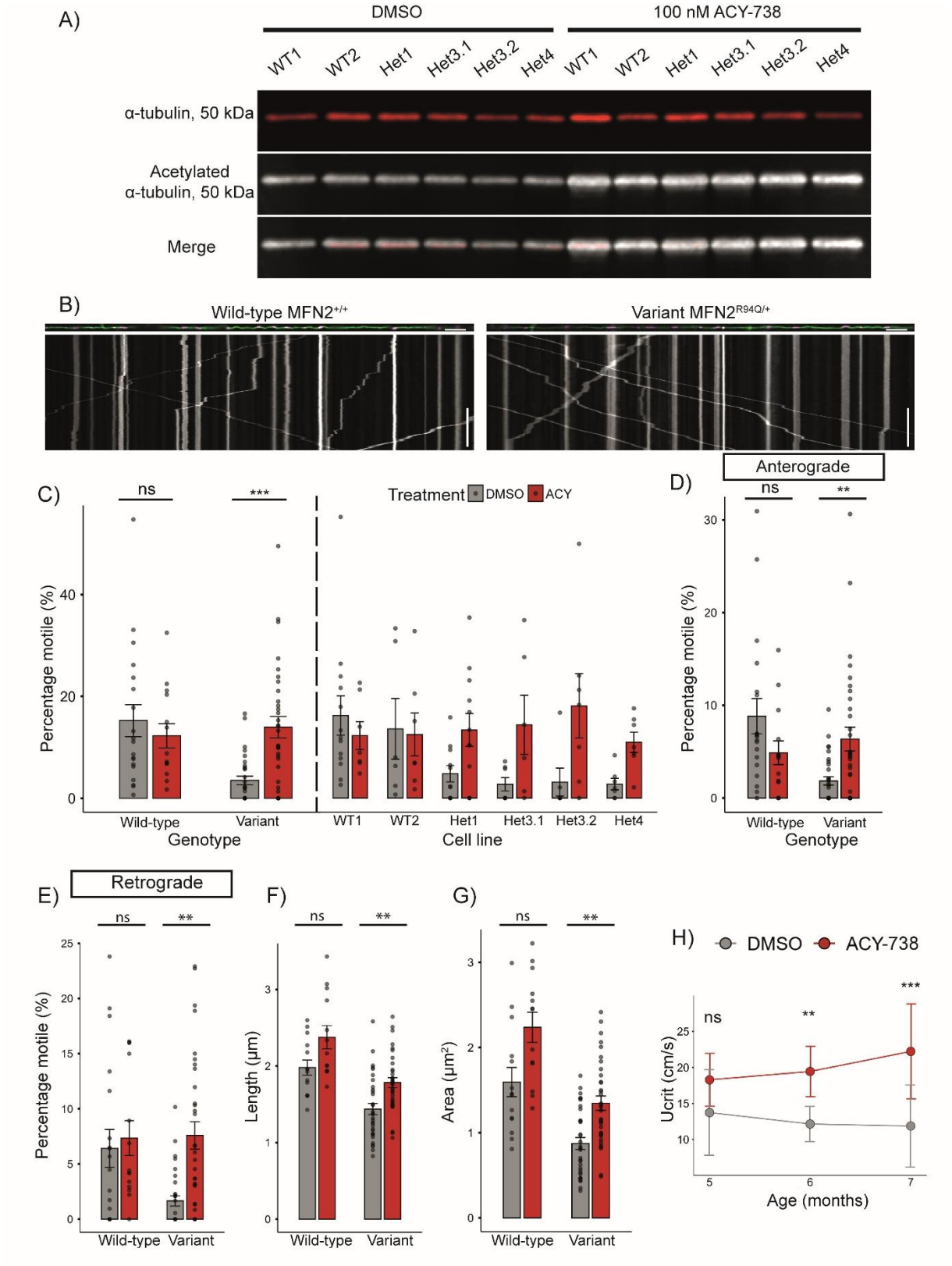

Figure 6: HDAC6 inhibition by ACY-738 partially rescues mitochondrial trafficking defect in axons of *MFN2*$^{R94Q/+}$ motor neurons and motor deficits in MFN2 variant zebrafish. (**A**) Western blot analysis of acetylated α-tubulin in Day 35 hESC-derived motor

neurons treated for 24 hours with either DMSO or 100 nM ACY-738. (**B**) Representative axon and corresponding kymographs of Day 36 wild-type and variant neurons after 24 hours of 100 nM ACY-738 treatment. Horizontal scale bar = 10 μm, vertical scale bar = 100 seconds. (**C**) The percentage of motile mitochondria in DMSO- or ACY-738-treated control and variant lines. (**D**) Percentage of anterograde mitochondria and (**E**) retrograde mitochondria in DMSO- or ACY-738-treated wild-type or variant lines. (**F**) Average length and area (**G**) of mitochondria in wild-type and variant *MFN2*$^{R94Q/+}$ hESC-derived motor neurons treated with DMSO or 100 nM ACY-738. Data shown as mean ± SEM with points representing average values from individual neurons in panels C–G. Statistical significance was calculated with a Mann-Whitney U test (C to E), N = 6 wild-type, 12 variant from 3 independent differentiations (*P<0.05; **P<0.01; ***P<0.001; ns, not significant). (**H**) The change in critical swimming velocity (U_{crit}) of *mfn2*$^{hu3528/hu3528}$ zebrafish between 5- and 7-months post-fertilisation following intermittent treatment by combined oral and immersion dosing with vehicle (1% DMSO) or ACY-738. Points and error bars represent mean and standard deviations of U_{crit} of individual fish measured at each time point (n = 8 vehicle-treated, n = 11 ACY-738-treated fish at 5 and 6 months post-fertilisation; n = 7 vehicle-treated, n = 11 ACY-738-treated fish at 7 months post-fertilisation). ns= non-significant, **p<0.01; ***p<0.001, two-way ANOVA with multiple comparisons between treatment groups at each time point.